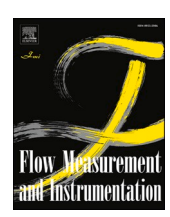
ELSEVIER

Contents lists available at ScienceDirect

#### Flow Measurement and Instrumentation

journal homepage: www.elsevier.com/locate/flowmeasinst



## Fluid-solid heat transfer analysis: In situ validation and calibration of a boiling meter using a combined experimental-numerical heat transfer approach

Abdelkabir Zaite <sup>a,\*</sup>, Himanshi Kharkwal <sup>b</sup>, Hervé Combeau <sup>o</sup>, Lounès Tadrist <sup>a</sup>

- <sup>a</sup> Université d'Aix-Marseille, CNRS, IUSTI, Marseille, France
- b Université Marie et Louis Pasteur, CNRS, Institut FEMTO-ST, F-25000, Besançon, France
- c Université de Lorraine, CNRS, Institut Jean Lamour, Nancy Cedex, France

#### ARTICLE INFO

# Keywords: Heat transfer Active heat sensor Natural convection In situ calibration Experiments Numerical simulations

#### ABSTRACT

To study and quantify the heat transfer between wall and fluid at the transition regime between natural convection and nucleate boiling, a boiling meter, incorporating two heat fluxmeters coupled with thermocouples, along with other components, was designed and built. This paper explores the methods used to calibrate and characterize this sensor under in situ conditions. The boiling meter has been experimentally investigated in a test cell for two configurations regarding the orientation of its largest faces with gravity: one vertical and the other one horizontal. The experimental results showed inconsistencies when compared to physical expectations. To address this problem, calibration of the boiling meter, using numerical simulations is performed with the CFD software Star-CCM+. These simulations were achieved considering the heat transfer at the scale of the whole test cell. The temperature and the heat transfer rate calculated at the two surfaces at the borders of each heat fluxmeter were compared with the experimental results. It was found that one thermocouple provided temperatures closer to those calculated at the outer end of a heat fluxmeter, while the other was closer to those at the inner end. Moreover, the numerical results revealed that the temperatures and fluxes at the boiling meter-liquid interface differed from the experimental measurements. The reasons for this discrepancy were identified and analyzed. As a result, the combination of experimental and simulation approaches allowed for a deeper understanding of the heat transfer measurements and results.

#### Nomenclature

Abbreviation	
Exp	Experimental
Sim	Simulated
FC-72	Perfluorohexane-Fluorinert fluid
Symbols	
C	Specific heat capacity (J/(kg.°C))
D	Diameter (m)
dt	Time step (s)
dx	Space step (m)
h	Convective heat transfer coefficient (W/(m <sup>2</sup> .°C))
g	gravitational acceleration (m/s <sup>2</sup> )
L	Length (m)
Nu	Nusselt number
P	Heat transfer rate (W)
p	Pressure (Pa)

(continued)

Prandtl number Rayleigh number Ra Volumetric heat source (W/m<sup>3</sup>) Temperature (°C)  $T_{ref}$ Temperature reference (°C) Time (s) Velocity (m/s) Subscripts 1 or 2 Fluxmeter numbers 1 or 2 а copper ехр Experimental FC FC-72 liquid fl Fluxmeter imp imposed

Inner

(continued on next page)

E-mail address: abdelkabir.zaite@gmail.com (A. Zaite).

https://doi.org/10.1016/j.flowmeasinst.2025.102905

Received 7 January 2025; Received in revised form 28 March 2025; Accepted 1 April 2025 Available online 2 April 2025

(continued on next column)

<sup>\*</sup> Corresponding author.

#### (continued)

j	Space node number (x)
out	Outer
S	Solid
Sim	Simulated
Tot	Total
ref	reference
rel	Relative
Greek symbols	
λ	Thermal conductivity (W/(m.°C))
ρ	Mass density (kg/m <sup>3</sup> )
$\varepsilon$	Measurement error
μ	Dynamic viscosity (Pa.s)
β	Thermal expansion coefficient
χ	(1/°C)
ν	Thermal diffusivity (m <sup>2</sup> /s)
	kinematic viscosity (m <sup>2</sup> /s)

#### 1. Introduction

#### 1.1. Context

Energy systems involve heat for energy conversion and/or heat dissipation. To ensure that these systems work efficiently, the heat generated must be controlled by creating appropriate fluidic architectures. Numerous techniques have been implemented to control heat transfer at the interface between a wall and a fluid [1]. These techniques, based on the boundary layers disturbances and/or the structuring of surfaces at the wall level, make it possible to enhance heat transfer [2].With the development of miniaturized components with increasingly complex functions, in microelectronics for example, the heat flux to be extracted can exceed 500 W/cm². Therefore, it is of the utmost importance to have heat removal methods tailored to these increasingly high heat flux. The use of phase change is one of the possible solutions to enhance heat transfer.

To develop such heat transfer enhancement techniques, it is necessary to be able to accurately quantify the heat transfer at fluid-wall interfaces. In this context, we have developed an experimental set-up equipped with a boiling meter, which we designed and built to characterize heat transfer in natural convection and nucleate boiling regimes.

Boiling meter calibration experiments were carried out in situ of the experimental set-up. Temperatures and heat transfer rates were measured at some locations with the goal of determining the heat transfer rate and the temperature at the surfaces of the boiling meter. Some of these measurements were inconsistent and difficult to interpret. Therefore, a validation calibration method has been implemented. This method is based on an approach involving experiments combined with modelling of heat, and momentum transfer in the experimental cell comprising the boiling meter, the fluid, and the envelope of the cell.

For heat flux measurement, there is no universal fluxmeter capable of measuring a heat flux at a wall-fluid interface, due to the variety of situations encountered. Existing sensors do not always benefit from metrological traceability due to the lack of appropriate reference standards, particularly in critical conditions such as unsteady heat transfer, low heat flux, etc.

As far as work on boiling is concerned, there have been several developments in heat flux and temperature measurement techniques. Given the complexity of the phenomena involved in boiling, most studies on heat transfer during boiling have focused on determining average parietal thermal characteristics. Several methods have been used to measure heat flux and wall temperature in steady state conditions. The first was proposed by Nukiyama [3] to determine the boiling curve. A thin electric wire was used as the heating element and as a sensor to measure the heat flux transmitted to the liquid and the wall temperature. In most of the work that followed, the measurement of the

heat flux on the wall was deduced by applying Fourier's law from the measurement of the longitudinal temperature gradient of the heating element of perfectly known thermal conductivity [4-7]). Over the last two decades, inverse methods have been developed to estimate heat flux and wall temperatures [8,9]. Infrared techniques have been tested for heat flux and temperature measurements [10-12]. However, they remain highly specific given the operating conditions under which they are used. In all cases, they require operating methods and resources that are often restrictive [13,14]. Specifically, using the infrared technique, a proper care should be taken for surface roughness, viewing angle and emissivity. For instance, a bright surface can reflect the incident radiations from the surrounding thus can alter the accuracy of measurements. However, as the emissivity of bright surface is very low, thus these surfaces are usually coated with a high emissivity paint and further for calculation, the surface is assumed to be gray with a particular emissivity. Therefore, to avoid inaccurate measurements, the emissivity value of the coating should be correct [15-18]. In fact, there is a particular difficulty in using an IR camera to study heat transfer phenomena in our case, because it can only be used in specific cases: thin heating walls or IR-transparent materials involving a wall at the edge of the cell. In addition to the difficulty of calibrating the measurement of wall temperature and heat flux emitted to the fluid for several reasons (emissivity, form factor, etc.).

The boiling meter offers some advantages for studying heat transfer in different configurations, such as the orientation of the heating wall and better control of measurements once calibration has been carried out

To avoid the complexities in calibration and measurement, a special device known as boiling meter was developed in this study, which gives the temperature and heat flux measurements in the boiling surface while providing the sufficient overheat for nucleation. This device is advantageous for studying heat transfer in different configurations, such as the orientation of the heating wall drowned in the liquid bulk with better control of measurements once calibration is complete.

However, before using the boiling meter, performing calibration is of utmost importance; since the factory calibration of heat flux sensors may be insufficient due to differences between calibration and real-world conditions, as well as installation-related errors that can impact the sensitivity of the sensor, as explained in Ref. [19]. In addition to that, in-situ calibration of heat flux sensor is mandatory, since, when a designed heat flux sensor is deployed in experiments, several challenges may arise, including the preparation methods and structural stability of the sensor, calibration techniques, errors in temperature measurement and thermal resistance layer properties, and varying work environments [20]. Thus, calibration with numerical simulations is important to visualise and thus calibrate the practical conditions to be employed on the sensor.

Furthermore, in a larger framework than boiling, several heat flux measurement techniques exist [10,21]. Given the difficulties in implementing heat flux measurement techniques at fluid-wall interfaces, coupled experimental-modelling-numerical simulation approaches are increasingly being implemented in the literature. The purpose of the following paragraph is to give a brief overview of the work carried out involving such an experimental-modelling approach.

In the study conducted by Xu et al. [22] numerical simulations were used to analyze a thin-film heat flux sensor affecting local flow and heat transfer in laminar flow over a flat plate. The results show that despite the small size of sensor, it significantly enhances local convective heat transfer by altering flow patterns and heat flux distribution on its surface. Thus, an empirical formula was developed to estimate the sensor's influence on heat transfer, such that it can be used in practical applications to minimize its effect on heat transfer.

The common objective of the reported work in this section is to enable the sensors developed to be better calibrated and to deliver more accurate measurements. Cortellessa et al. [23] proposed a new means of calibrating heat fluxmeters for building heating applications. They

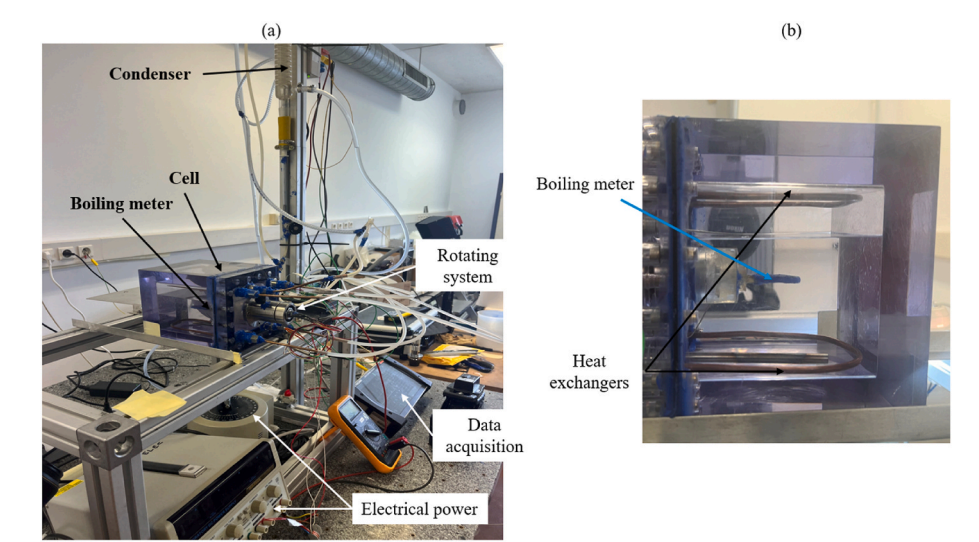


Fig. 1. Photo of the experimental system containing the test cell, the connections to the cooling system, the condenser, as well as the electrical generators for the heater and the data acquisition system. (b) Photo of the plexiglass cell.

examined the metrological performance of this device operating under critical conditions such as the low heat flux regime and low thermal conductivity values. In addition to experiments, they carried out detailed numerical simulations. These simulations were used to validate the results obtained from the measurements. The digital model developed enables the calibration system to be analyzed under different operating conditions. The numerical results have enabled these authors to better control heat flux measurements.

Arpino et al. [24] carried out a numerical study to design a heat fluxmeter calibration system. Predictions of the metrological performance of such a system were estimated by modelling and numerical simulation. Based on the numerical results, the authors designed and produced a sensor for measuring the thermal conductivity of insulating materials and calibrating a fluxmeter using a thermal protection to reduce lateral heat losses. Numerical studies have shown that fine temperature control of thermal protection is necessary to minimize the uncertainty of the heat flux generated.

Numerical and experimental analysis of a heat fluxmeter for low to moderate heat fluxes  $(10-100~W/m^2)$  was conducted by Arpino et al. [25]. The temperature distribution and heat flux uniformity were studied by COMSOL Multiphysics®. The results show excellent heat flux uniformity in the measurement section with deviations below 0.4 %. Using both numerical and experimental methods, the study concludes with the development of an improved prototype with superior heat flux uniformity.

Mariya N. Polyashchenkova et al. [26] studied the influence of different technological factors on the calibration of the heat flux sensor output signal. To do this, they used numerical simulation with the ANSYS software.

#### 1.2. Purpose of this study

As can be seen, there is no universal sensor for measuring heat flux, given the diversity of situations in which heat flux measurement is required. To our best knowledge, we are not aware of previous investigations on calibration sensors for measuring heat transfer characteristics in permanent and transient regimes. The aim of our study is to use a boiling meter, an active sensor, to quantify heat transfer between a heated wall and a fluid. This sensor has been the subject of previous work, which demonstrated its ability to detect the onset of nucleate boiling (ONB) and establish characteristic heat transfer curves for natural convection and nucleate boiling regimes for different wall orientations [27]. Recent calibration tests with a new generation boiling

meter have highlighted inconsistencies in heat transfer results. Therefore, we have initiated a calibration procedure that considers the effects of natural convection in steady and unsteady state regimes. We aim to determine the instantaneous heat transfer rate and temperatures at the wall-liquid interface under natural convection and nucleate boiling regimes. For the nucleate boiling investigations, 800 µm thick copper discs were glued to the faces of the boiling meter to create nucleation sites of controlled depth and opening diameter. Captec fluxmeters [28], consisting of a thermocouple and a thermopile, are positioned in between the copper discs and the heater. They provide access to the temperatures and heat transfer rate crossing the fluxmeters. As a result, it is not possible to directly access the heat transfer rate and temperatures at the fluid-wall interface. To achieve this, we implemented a calibration validation approach for the boiling meter by carrying out modelling and numerical simulation to complement the experimental approach. The modelling considers coupled convective-diffusive heat transfer in the fluid and conductive heat transfer in the boiling meter and the cell envelop.

The proposed methodology is applicable for calibrating any active heat transfer sensor. Its originality lies in the fact that it accounts the physical phenomena occurring at different length scales (from  $\mu m$  to cm length) in the sensor and its environment.

In the second section, we present the experimental set-up, including the various components, the measurement protocol, and the experimental results. The heat transfer rate measurement technique and the experimental results obtained using the boiling meter are described. Two orientations of the boiling meter were investigated. A vertical orientation, parallel to gravity, corresponds to a symmetrical heat transfer situation on the two sides of the boiling meter. A horizontal orientation is perpendicular to gravity, in this case, the heat transfer is asymmetrical. On the upper face, a natural convection regime can take place in the fluid, while on the lower face, a heat conduction regime predominates.

Based on the experimental results, we show that there are inconsistencies in the heat transfer rate and temperature measurements that cannot be explained by the experimental analysis alone. For this reason, a complementary approach based on the modelling of the heat transfer within the cell has been implemented.

The third section is devoted to the modelling and numerical simulation of the heat transfer phenomena in the cell. The numerical simulations were carried out using the commercial code Simcenter STAR-CCM+ (18.06.006) [29]. The steps involved in carrying out the simulations and obtaining the numerical results are described in detail.

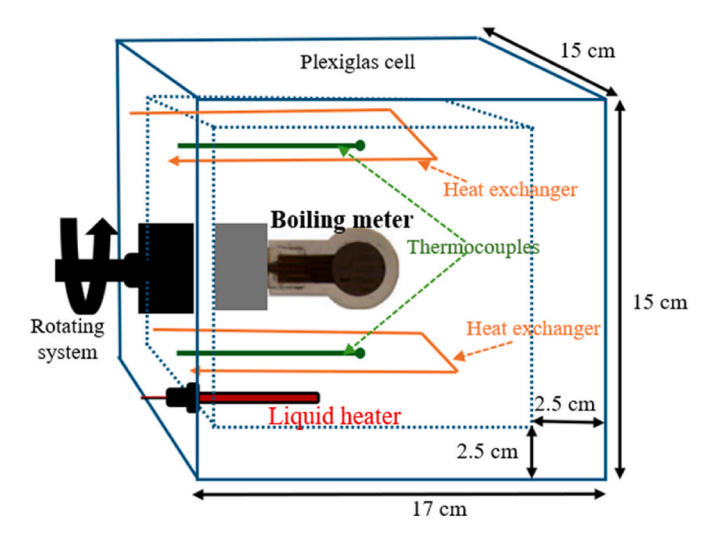


**Fig. 2.** Schematic view of the plexiglass cell with the main components: the boiling meter with the rotating support, the thermocouples, the heat exchangers, and the liquid heater.

Table 1 Thermophysical properties of the FC-72 [30] and the air over a temperature range from 20 to 40  $^{\circ}\text{C}.$ 

Fluid	Density (kg/m³)	Dynamic viscosity (Pa.s)	Thermal conductivity (W/(m.°C))	Specific heat capacity (J/(kg.° C))	Thermal expansion coefficient (1/°C)
FC- 72	1649	$4.431.10^{-4}$	0.052	1102	$1.664.10^{-3}$
Air	1.19	$1.85.10^{-5}$	0.026	1003.62	0.0033

In the fourth section the numerical and experimental results are compared. Thanks to the analysis of the experimental results in combination with the numerical results, we show that it is possible to explain and interpret the inconsistencies found in the experimental results. We also show that the heat transfer rate and the temperature at the fluidwall interface can only be accurately determined with the support of the numerical simulation tool.

Finally, the fifth section is devoted to the conclusion and perspectives.

#### 2. Experimental setup, protocol, and results

The experimental set-up used to calibrate the boiling meter was

designed and built to study fluid-wall heat transfer for natural convection and nucleate boiling regimes. We describe the experimental set-up components, and the experimental protocol adopted to calibrate the boiling meter. Then the main results concerning the temperature and heat transfer rate measurements to characterize and calibrate the boiling meter are presented.

#### 2.1. Description of the experimental setup

This section describes the experimental loop including the cell and devices used in the experiments.

#### 2.1.1. Test cell configuration

Figs. 1 and 2 show the photos and a schematic view of the components of the experimental set-up. The experimental setup consists of a parallelepiped-shaped plexiglass cell. The fluid compartment volume in this cell is 10 cm high and wide, 12 cm long with a wall thickness of 2.5 cm. The working fluid used is the Perfluorohexane-Fluorinert liquid (FC-72). It fills two-thirds of the cell. One-third of the last upper part is filled with air. The thermophysical properties of the two fluids (FC-72 and air) are given in Table 1. These properties can be considered as constant in the domain of temperature [20 °C, 40 °C] corresponding to the experiments reported in this paper.

The cell is equipped with two thermocouples K type to measure the temperature in the liquid and the gas phases. A heating cartridge, placed in the lower part of the cell is used to heat the liquid to the desired temperature. The cartridge is connected to an electrical generator. Two water heat exchangers connected to a cold-water tank and controlled by valves enable to maintain the liquid and gas phases at the desired temperatures.

The boiling meter, the key element for studying fluid-wall heat transfer, is installed in the center of the cell. It is attached to a cylindrical rod held to the wall by a system that allows it to be rotated from 0 to  $\pi$ , thereby orienting the walls of the boiling meter at the desired angle with respect to gravity. The boiling meter is equipped with 2 heat fluxmeters and 2 thermocouples whose locations are given in the next section.

A data acquisition system "Multichannel Recorder DAS240BAT, SEFRAM" measures and records temperatures, imposed power, and heat transfer rate, with a time step of 1s. It allows monitoring measurements of the electrical power supplied by the generator, the heat transfer rate, the temperatures at the Heat fluxmeters, and the temperatures of the FC-72 at different locations.

#### 2.1.2. Description of the boiling meter

A first version of the boiling meter was designed in the laboratory [31]. The version used in this project has been manufactured by the Captec company [28]. Fig. 3 shows an exploded view of the boiling meter with its elements. By design, its geometry features a plane of

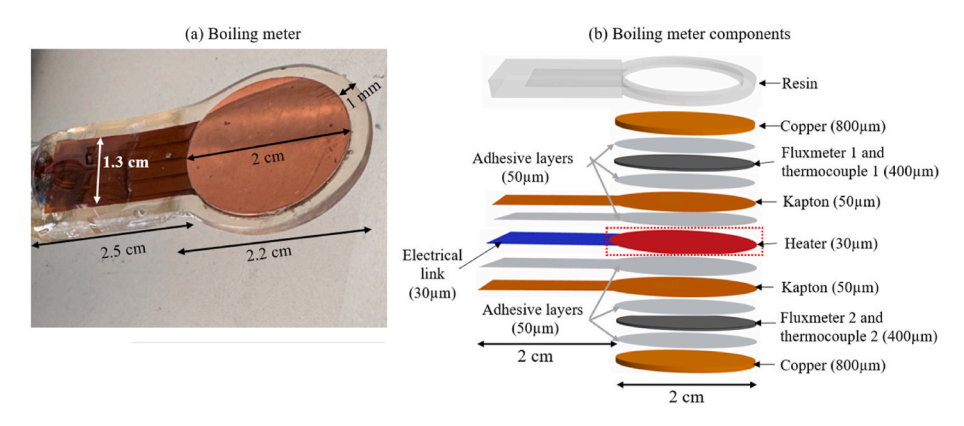


Fig. 3. Overview of (a) the boiling meter and (b) its components (the heater in the center with the electrical link, the two layers of Kapton, the two heat fluxmeters, the two copper discs, the resin band, and the adhesive layers).

**Table 2**Thermophysical properties of the cell and the boiling meter components [27].

Material	Thickness (µm)	Diameter (cm)	Thermal conductivity (W/(m.°C))	Specific heat capacity (J/(kg.°C))	Density (kg/m <sup>3</sup> )
Plexiglass	2.5.10 <sup>4</sup>	_	0.19	1470	1190
Copper	800	2	398	386	8900
Heat fluxmeter [28]	400	2	0.4	693	4920
Heater film (constantan)	30	2	19.5	390	8900
Adhesive (Resin)	50	2	0.25	1000	1000
Resin	50	2.4-2	0.25	1000	1000
Kapton	50	2	0.2	1090	1420

symmetry parallel to its large faces and passing through its center (Fig. 3 (b)). It consists mainly of two copper discs on the external sides, two circular heat fluxmeters and temperature sensors, two layers of Kapton, and a heating resistor in the center. These elements are assembled using adhesive layers and coated with an insulating resin to minimize lateral heat losses. The components are assembled as follows: in the center, a heating resistance, made of constantan wire embedded in glue, is installed between two layers of Kapton, providing electrical insulation. Next, a circular Thery-type heat fluxmeter is glued on each side. On the other side of the heat fluxmeters, copper disks are glued. These elements are then surrounded by resin used as a thermal insulator.

The electric power imposed to the heater is determined by the product of the voltage measured across the heater with a micro voltmeter by the value of the electric resistance of the heater which is equal to 20  $\Omega$ . The accuracy of the micro voltmeter is equal to 5  $\mu$ V, while the value of electric resistance is known with an uncertainty of  $\pm 0.1~\Omega$ . Therefore the uncertainty of the electric power is  $\pm 0.005~W$ .

The circular heat fluxmeters used are tangential thermal gradient fluxmeters [32]. They consist of a planar thermopile inserted between two Kapton films and then copper films to create a tangential thermal gradient on which the principle of measuring the heat transfer rate through the heat fluxmeter is based. A great deal of work has gone into developing this type of sensor (Thery et al. [32], Yala [33], Gidik [34], Thureau [21]). To the best of our knowledge, this sensor is calibrated under steady-state conditions for each sensor produced. The two sensors making up the boiling meter have a calibration constant of 2.94  $\mu V/(W/m^2)$  for one and 2.67  $\mu V/(W/m^2)$  for the other. Accuracies range from  $\pm 3$  % (Captec [28]). For response time, the value claimed by the manufacturer is 150 ms. We have not found a reference specifying how this value was established. The accuracy of the T-type temperature sensors incorporated in the heat fluxmeter is  $\pm 0.1$  °C. The thermocouples have been calibrated by measuring the liquid/vapor equilibrium temperature of FC-72 at the atmospheric pressure. The difference of the measure with the tabulated value was 0.1 °C. The equivalent thermophysical properties of the heat fluxmeters were evaluated by considering the properties of the heat fluxmeter components arranged in series.

According to the Captec company, that made the heat fluxmeter, the thermocouple is embedded along the symmetry axis and at approximately 160 µm in depth from the upper surface. In the following, we will refer to the two heat fluxmeters and their two associated thermocouples as 1 and 2. Dimensions and thermophysical properties of the boiling meter elements are presented in Table 2. It's important to note that the equivalent thermophysical properties of the heat fluxmeter were calculated using the thermal resistance method. This choice can be explained by the composition of the device, made up of components arranged in multilayers, and by its low thickness (400 µm). The values obtained are similar to those given by the manufacturers Captec [28] and FluxTec [35] Furthermore, the numerical simulations presented in the rest of this article using these properties give results in very good agreement with the measurements. We therefore consider these equivalent physical properties to be sufficient to account for heat transfer in the fluxmeter.

#### 2.2. Protocol

In this work, experiments were carried out to quantify the heat transfer between a heated wall and a liquid under natural convection, and to analyze the measurements provided by the heat fluxmeters. The adopted experimental protocol is presented in this section. The experimental cell was filled to two-thirds with FC-72 liquid and covered with an air canopy. The experiments were carried out in subcooled conditions at ambient temperature and atmospheric pressure for two configurations of the boiling meter corresponding to two different orientations of the boiling meter with respect to the gravity.

In the first configuration, the boiling meter was installed vertically (its largest faces are parallel to the gravity direction) so that as the boiling meter geometry is symmetrical the heat and momentum transfers in the liquid can be expected to be symmetrical with respect to the plane of symmetry of the boiling meter. In this configuration, the heat transfer rate and the temperature sensors on either side of the boiling meter must give identical results. For this case, once thermal equilibrium had been reached, the electrical heater within the boiling meter was supplied with 0.325 W of electrical power for 90 s. This time corresponds to the time when the values measured by two heat fluxmeters tend towards a constant value over time. The power is then manually increased to 0.864 W for 100 s in the same way. The last power tested was 1.326 W for 90 s.

In the second configuration, the boiling meter device is placed horizontally (its largest faces are perpendicular with respect to the gravity direction). In this case, the liquid motion is different on each side of the boiling meter. The heat flux transmitted to the liquid through the upper wall can give rise to natural convection. In contrast, the heat transfer through the lower wall gives rise mainly to a weak natural convection regime mainly driven by heat conduction. From the initial time to 30s, the electric power of the heater is turned off. The thermocouples in the boiling meter indicate a temperature of 23 °C while the FC-72 temperature is at 21.8 °C corresponding to the ambient temperature. The electrical powers generated by the heater are 0.325 W from t = 30s to t = 208s, 1.431 W from t = 209s to t = 395s, and 2.66 W from t = 396 to t = 540s, respectively. For each power, one waits until the temperature becomes almost constant with time.

Both experiments approaches were carried out under normal conditions (atmospheric pressure and ambient temperature). During these experiments, the heating resistor of liquid was not operated. Both heat exchanger valves were closed, and the temperature of FC-72 was identical to that of the ambient air and water in the two heat exchangers.

#### 2.3. Experimental results

#### 2.3.1. 1st configuration: vertical position

Fig. 4(a) and (b), and Fig. 4(c) present, respectively, the time evolution of the experimental temperatures and heat transfer rates obtained by the two thermocouples ( $T_{exp1}$ ,  $T_{exp2}$ ) and the two heat fluxmeters 1 and 2 ( $P_{exp1}$ ,  $P_{exp2}$ ), as well as the relative gaps between the measured heat transfer rate and the imposed power ( $P_{imp}$ -( $P_{exp1}$ +  $P_{exp2}$ )).

The changes over time in the temperatures of the thermocouples 1 and 2 of the boiling meter are plotted in Fig. 4(a) for the periods corresponding to the three power settings (0.325, 0.861, and 1.326 W).

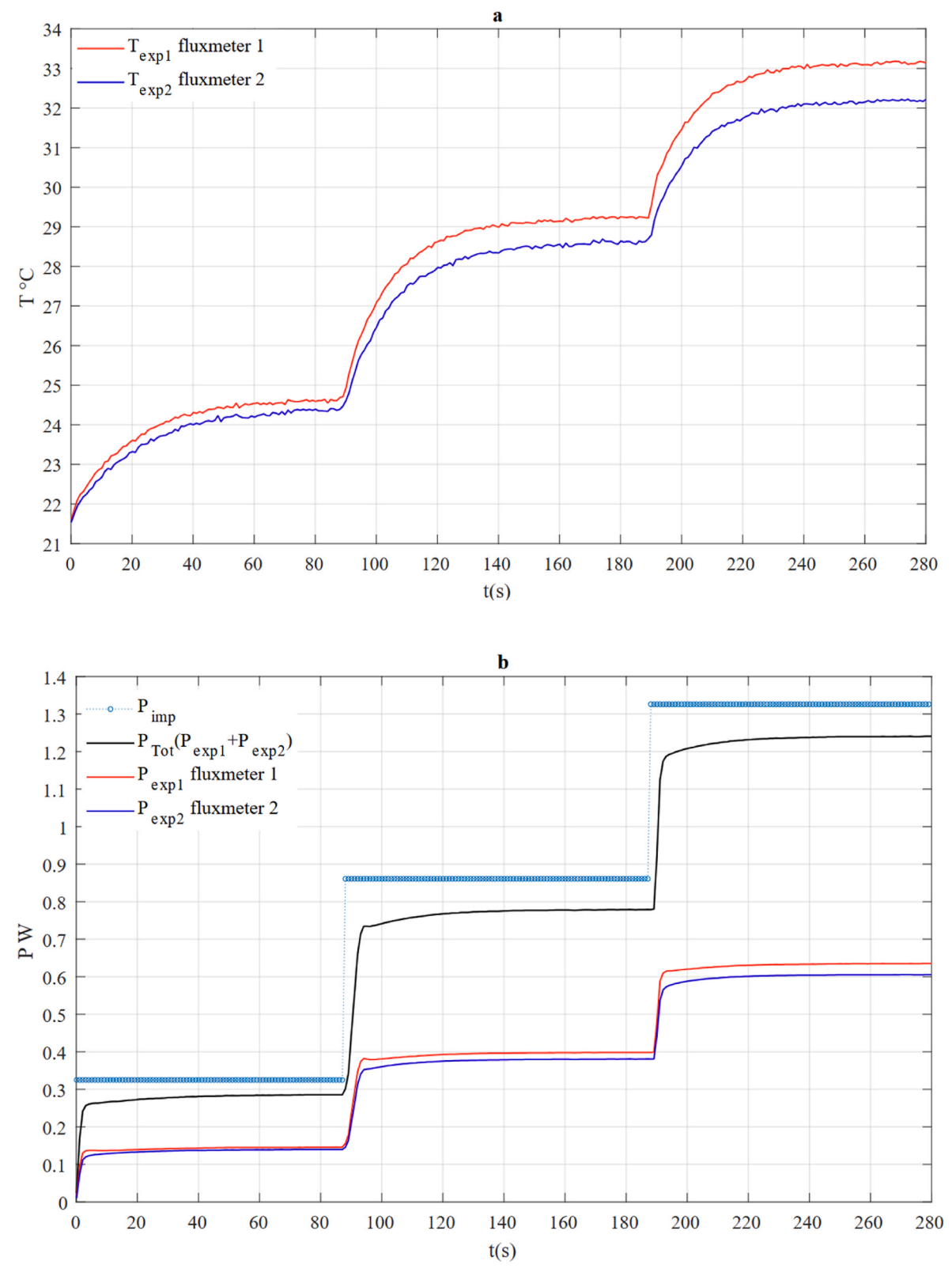


Fig. 4. Time evolution of the (a) temperatures  $T_{exp1}$  and  $T_{exp2}$ ; (b) time evolution of the heat transfer rates  $P_{exp1}$  and  $P_{exp2}$  and of the sum of both heat transfer rates  $P_{exp1} + P_{exp2}$  for the imposed powers of 0.325, 0.861, and 1.326 W in the vertical configuration. (c) Time evolution of the relative gaps between the two heat transfer rates  $\delta P_{21,rel}$  as well as the relative gaps of the total heat transfer rate ( $P_{exp1}$  and  $P_{exp2}$ ) to the imposed power ( $P_{imp}$ ).

Each time the heating power is increased, the two temperatures rise towards a plateau which is practically reached at the end of each exploration period. Despite the symmetry of the boiling meter geometry and the configuration concerning natural convection, there is a temperature difference between the two sensors that increases with the power applied. In the quasi-steady state regime, the difference ( $T_{exp2}$ -

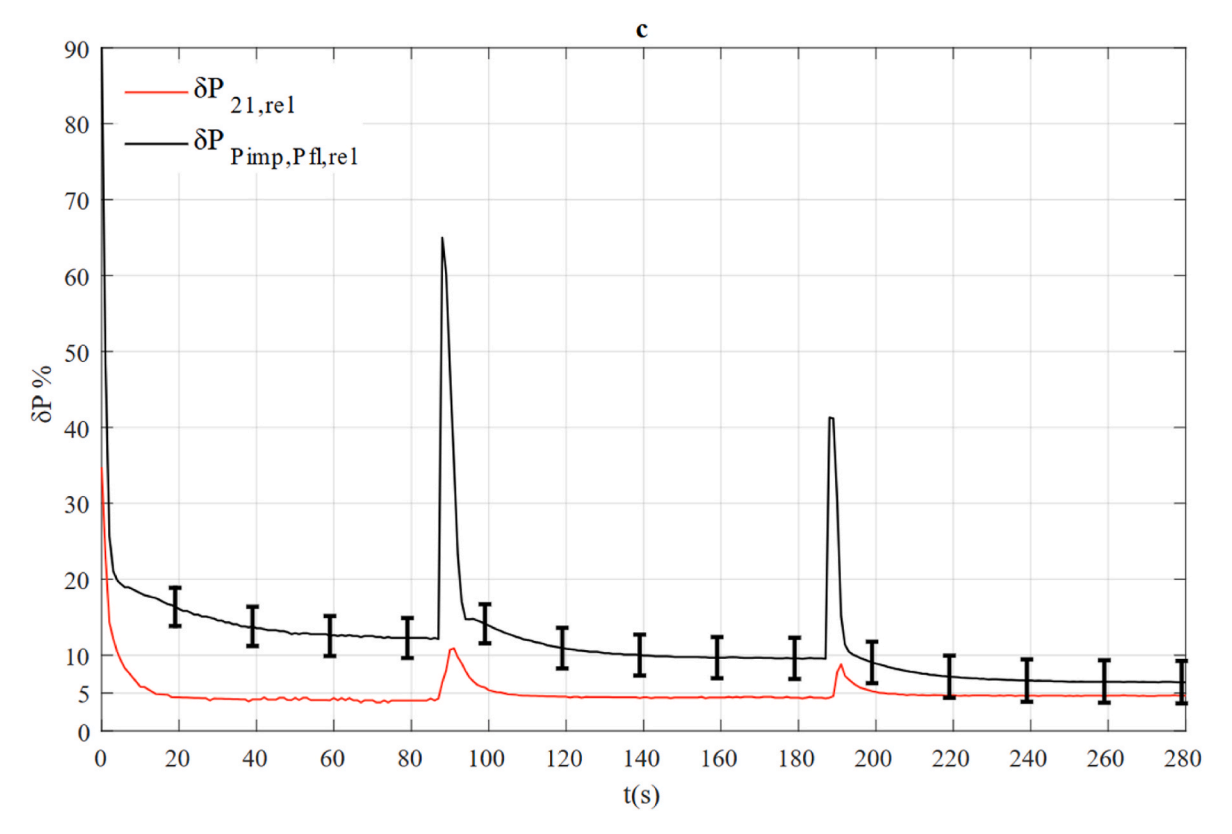


Fig. 4. (continued).

 $T_{exp1})$  is equal to 0.35, 0.75, and 1.05  $^{\circ}C$  respectively for the imposed powers 0.325, 0.864 and 1.326 W. This difference is greater than the accuracy of the two temperature sensors, which is equal to 0.2  $^{\circ}C$ .

The temporal evolution of the measured heat transfer rates  $P_{exp1}$  and  $P_{exp2}$  by the heat fluxmeters 1 and 2, the sum of these two heat transfer rates ( $P_{exp1}+P_{exp2}$ ) and the power supplied ( $P_{imp}$ ) to the heating element are plotted in Fig. 4(b). The relative difference between the two fluxes defined as  $\delta P_{21,rel} = \frac{P_{exp} - P_{exp} - 1}{P_{exp} - 1}$  in quasi-steady state regime does not exceed 5%. As reported in the previous section, the error  $\varepsilon = \frac{\Delta P_1}{P_1}$  of the heat fluxmeters is  $\pm 3$ %.  $\delta P_{21,rel}$  is significantly larger at the start of each period of imposed power (Fig. 4(c)). It reaches 15% for the lowest value of the imposed power at the beginning of the period. This suggests that the location of the sensitive parts of the heat fluxmeters are not at the same distance from the plane of symmetry of the boiling meter. The sum of the heat transfer rates ( $P_{exp1}+P_{exp2}$ ) is also shown in Fig. 4(b). In the steady state,  $P_{exp1}+P_{exp2}$  differs from the imposed power ( $P_{imp}$ )which is also shown in this figure. The evolution of the relative deviation

also shown in this figure. The evolution of the relative deviation 
$$\delta P_{Pimp,Pfl,rel} = \left| \frac{P_{imp} - (P_{exp} + P_{exp} + 2)}{P_{imp}} \right| \text{ is shown in Fig. 4(c). The error of this}$$

relative deviation is equal to  $\varepsilon_{exp} = \varepsilon \frac{\left(P_{exp\ 1} + P_{exp\ 2}\right)}{P_{limp} - \left(P_{exp\ 1} + P_{exp\ 2}\right)}$ . Error bars corresponding to  $\varepsilon_{exp}$  are placed on the  $\delta P_{Plimp,Pfl,rel}$  curve. The positive values of  $\delta P_{Plimp,Pfl,rel}$  are greater than the error. It means that the difference between the imposed power and the sum of the two measured heat transfer rates is significant.

Under these conditions, it can be considered that other effects may be responsible for these differences in heat transfer rate, such as lateral losses within the boiling meter. These effects will be explored in section 4 of this paper.

#### 2.3.2. 2nd configuration: horizontal position

The second series of experiments focus on the fluid-wall heat transfer in the horizontal configuration of the boiling meter for three imposed

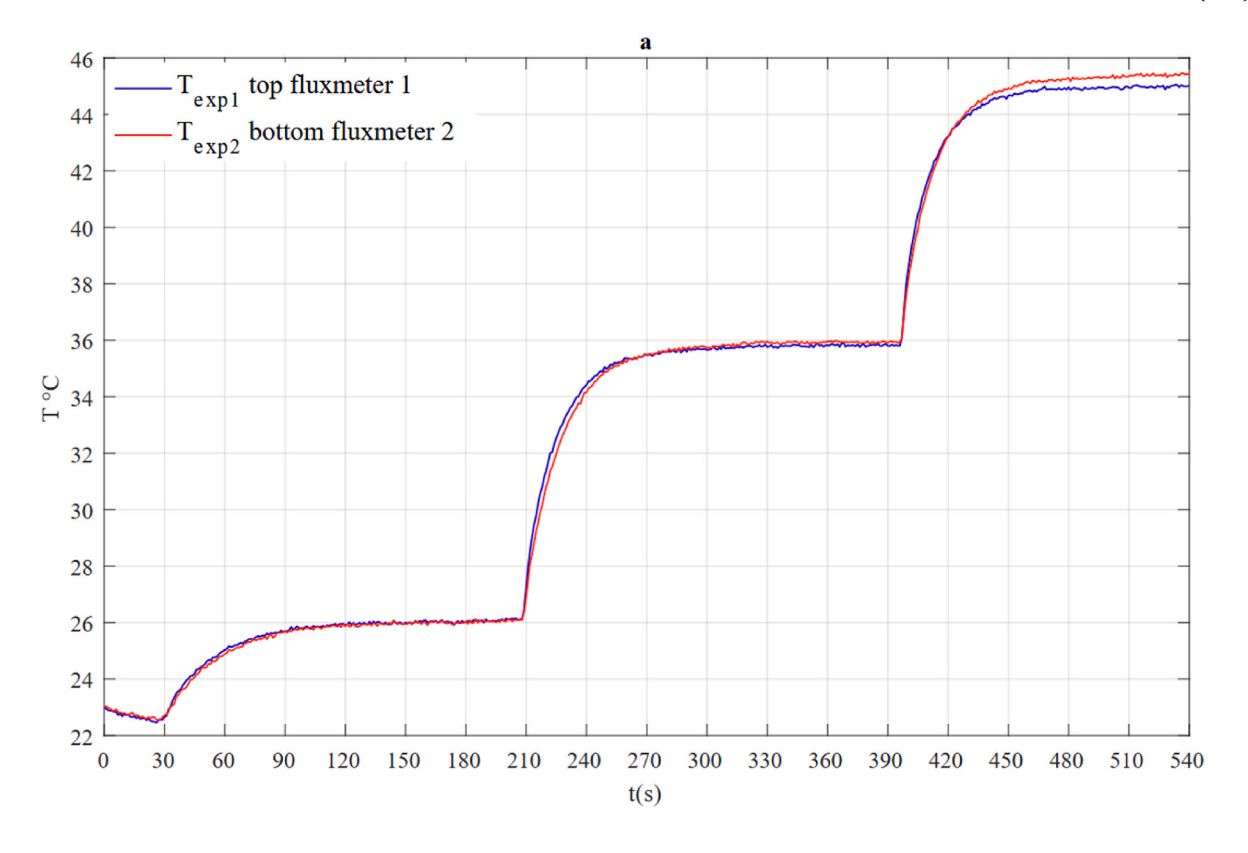
powers (0.325, 1.431, and 2.264 W). In this configuration, the heat fluxmeter  $P_{exp1}$  and the thermocouple  $T_{exp1}$  are located on the upper face of the boiling meter, and the heat fluxmeter  $P_{exp2}$  and the thermocouple  $T_{exp2}$  on the lower face.

Fig. 5(a) shows the temporal evolution of the temperatures measured by the thermocouples  $T_{exp1}$  and  $T_{exp2}$  installed in the heat fluxmeters for the whole time of the experiment. During the first 30s, the imposed power was equal to zero (the electrical generator was turned off). The two temperatures T<sub>exp1</sub> and T<sub>exp2</sub> decrease as the boiling meter starts with a temperature of 23 °C while the FC-72 is at a temperature of 21.8 °C. The temperature profiles given by the thermocouples  $T_{\text{exp1}}$  and Texp2 give almost identical values whatever the imposed power. Deviations are, however, observed for the case of the highest imposed power ( $P_{imp} = 2.264$  W). In terms of heat transfer rate, the heat fluxmeter 1 (pointing upwards) gives higher heat transfer rate (Pexp1) values than the fluxmeter 2 ( $P_{exp}$ 2) (Fig. 5(b)). Differences in heat transfer rate are observed whatever the imposed power, as shown in Fig. 5(c). These differences in heat transfer rate values can be explained by the fact that natural convection is generated on the upper side while on the lower side a conduction regime predominates.

The difference between the total heat transfer rate measured by the two heat fluxmeters  $(P_{exp1}+P_{exp2})$ , is less than the power dissipated at the center of the boiling meter  $P_{imp}$  under quasi-stead state conditions. The relative difference is between 11.8 % and 13 % for the first imposed power (0.325W), and around 7.6 and 8.1 % respectively for the imposed powers of 1.431 and 2.66W. This difference, as can be seen in Fig. 5(c)–is always greater than the total measured heat transfer rate  $(P_{exp1}+P_{exp2})$ . This result is undoubtedly due to lateral losses. This assumption will be checked in section 4 of the paper.

#### 2.3.3. Synthesis of the experimental results

These results reveal a few inconsistencies. First, the temperatures and heat transfer rates obtained in a symmetrical configuration (vertical configuration of the boiling meter) are asymmetrical. Second, in asymmetrical configuration of the boiling meter) are asymmetrical.



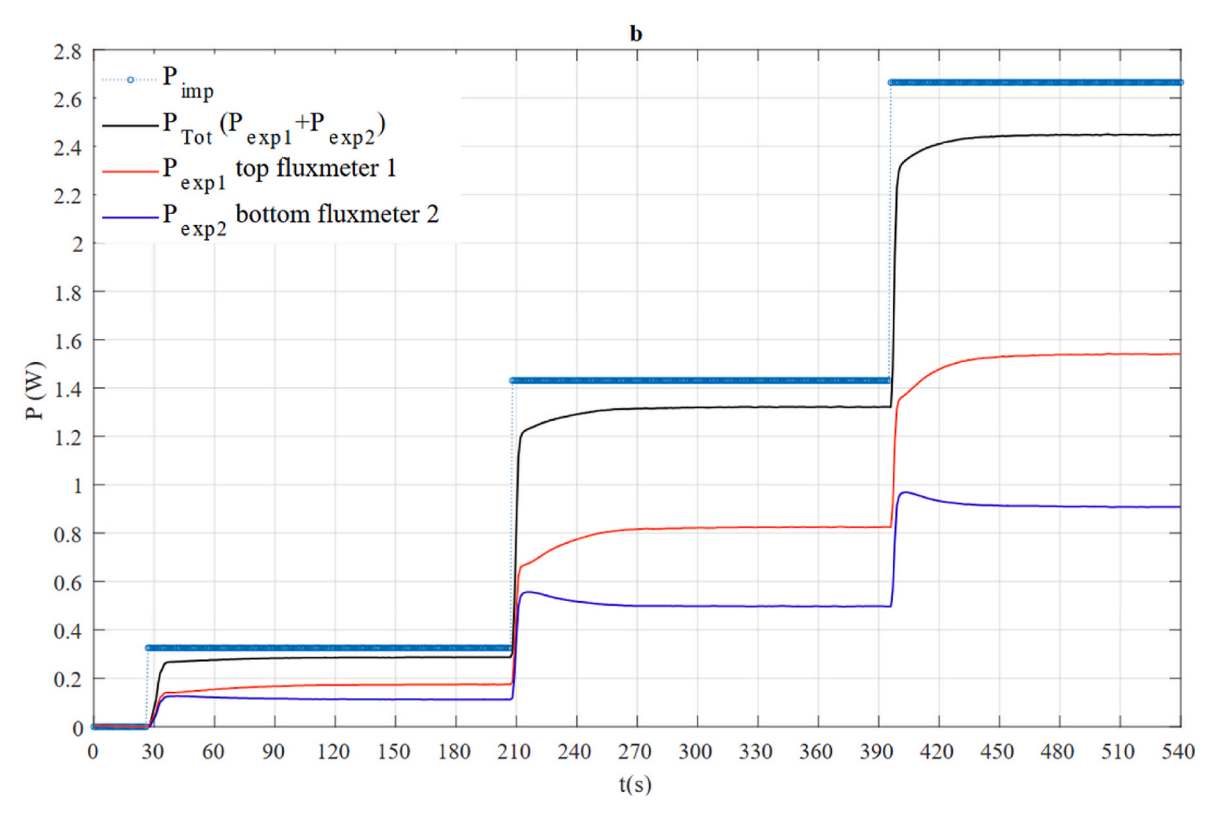


Fig. 5. Time evolution of (a) the temperatures  $T_{exp1}$  and  $T_{exp2}$  (b) the heat transfer rates measured by the top and bottom heat fluxmeters ( $P_{exp1}$  and  $P_{exp2}$ ) as well as the sum of both heat transfer rates  $P_{exp1} + P_{exp2}$  for the heat power of 0.325, 1.431, and 2.264 W in the horizontal configuration. (c) Time evolution of the relative gaps between the two heat transfer rates  $\delta P_{21,rel}$  as well as the relative gaps of the total heat transfer rate ( $P_{exp1} + P_{exp2}$ ) to the imposed power ( $P_{imp}$ ).

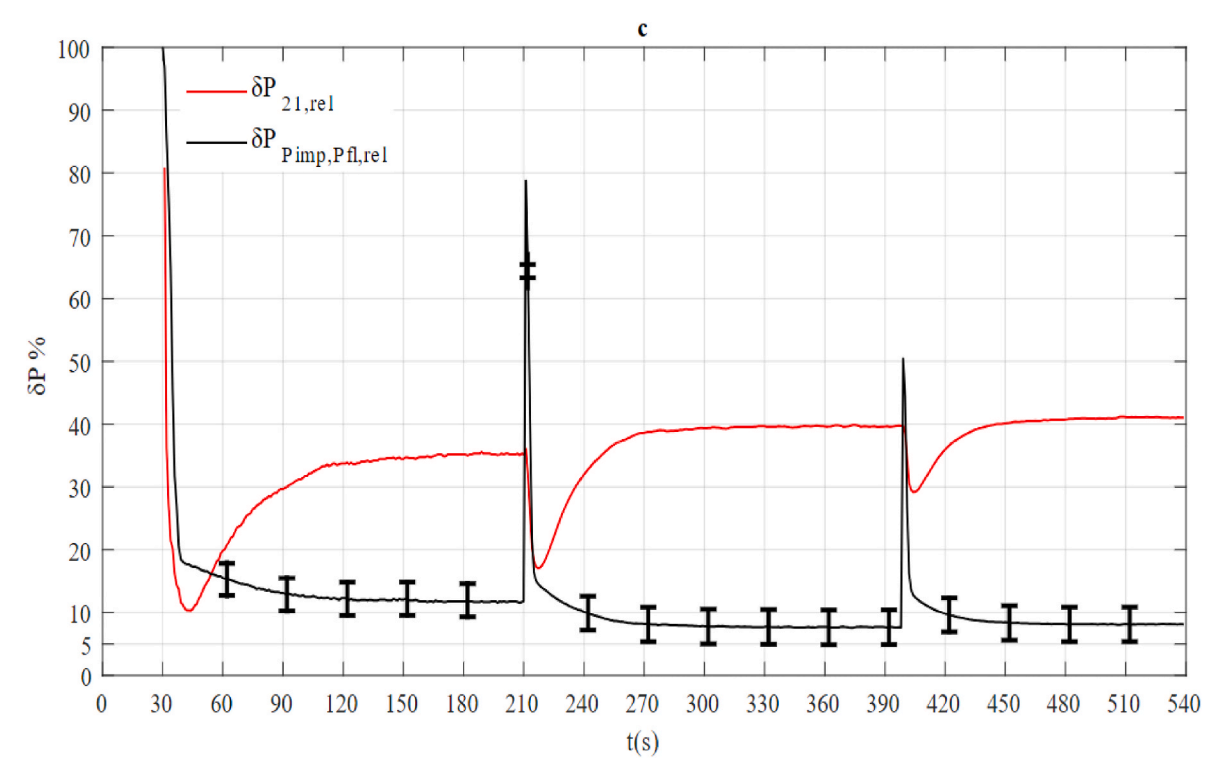
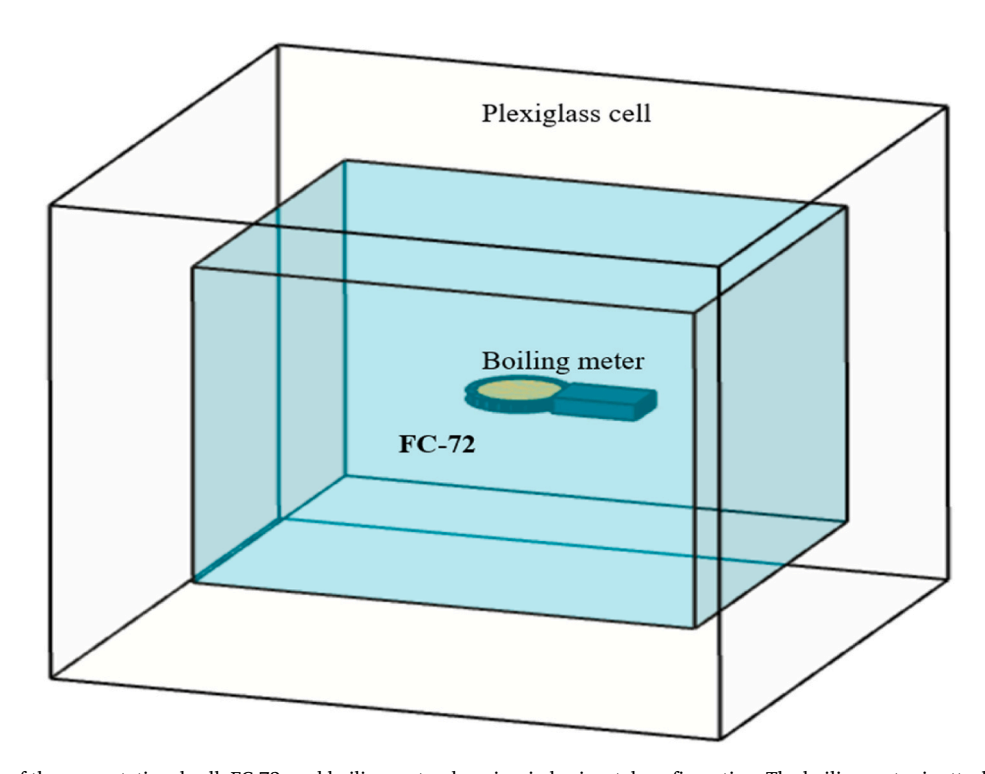


Fig. 5. (continued).



**Fig. 6.** Geometric view of the computational cell, FC-72, and boiling meter domains, in horizontal configuration. The boiling meter is attached to the side wall via a hollow cylinder through which the electrical wires connecting the various sensor components pass. This connection to the wall has been neglected as a first approximation to simplify the simulations.

metrical configuration (horizontal configuration of the boiling meter), the thermocouples  $T_{\rm exp1}$  and  $T_{\rm exp2}$  indicate almost similar temperatures. Third, the imposed power is systematically higher than the heat transfer rate measured by the heat fluxmeters  $P_{imp} > (P_{exp~1} + P_{exp~2})$  whatever the operating conditions are (imposed power, geometrical configuration). As we can see, all these issues cannot be resolved based on the

experimental approach alone. The spatial resolution of temperature and heat transfer rate measurements does not allow us to better interpret these results and access information on heat transfer at wall-fluid interfaces.

To resolve the inconsistencies of these measurements and explain the obtained results, we have implemented a complementary approach. This

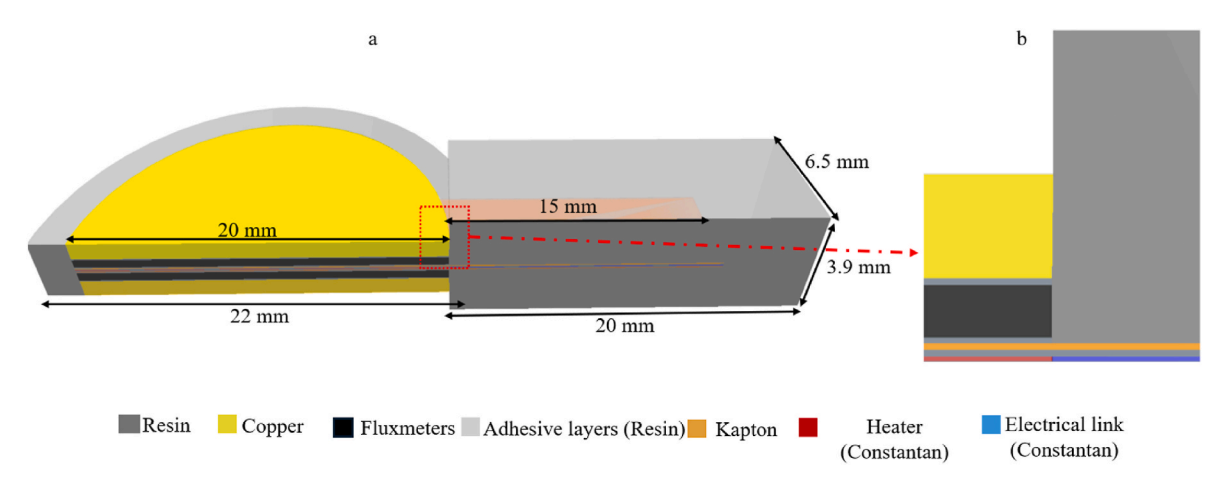


Fig. 7. Geometric view of the boiling meter: (a) half of the boiling meter and (b) a front view of its components.

approach is based on the numerical modeling of the coupled heat transfer phenomena in the boiling meter and inside the fluid in which natural convection structures develop. This approach is presented in the next section.

#### 3. Mathematical modeling

The complex geometry, the confinement effect and the transient regime make impossible to know in advance the degree of accuracy of results obtained from correlations proposed in the literature for the determination of the heat flux at the surface of the boiling meter. This is why we have chosen to carry out a direct numerical simulation in the measurement cell, considering the conjugated heat transfers in the boiling meter and the fluid. These phenomena occur at several length scales for 1 µm to several centimeters. Following this comment, the experimental apparatus, including the test cell and the boiling meter has been numerically reproduced using 3D transient simulations. The numerical model developed aims to investigate coupled liquid/solid heat transfer and complete the investigation of the experimental results.

On one hand, these simulations are designed to determine the origin of the temperature and heat transfer rate asymmetry observed in the experimental results. On the other hand, they aim to identify the causes of the heat transfer rate losses noted in the two configurations (vertical and horizontal) and to analyze the evolution of the temperature and the heat transfer rate at the interface between the boiling meter and the FC-72 liquid.

Accordingly, numerical simulations were carried out using the boiling meter in vertical and horizontal configurations.

#### 3.1. Geometries description

Fig. 6 presents the cell geometry containing the FC-72 liquid and the boiling meter in the horizontal configuration. The cell size is identical to that used in the experiment.

In the experiments, the cell is partially filled with FC-72 at two-thirds and the upper part is filled with an air canopy. Several simulations accounting for this air canopy have been performed and compared with simulation for similar conditions considering the cell fully filled with FC-72. No differences in the heat transfer inside the boiling meter and its vicinity were observed between these two configurations. As the simulations with the cell fully filled with FC-72 are shorter, we decided to neglect the air canopy. The effect of the two heat exchangers, the cell thermocouples, and the heating resistance of the liquid is considered negligible. Half of the boiling meter model, with the various adhesive layers and the insulating resin strip, is shown in Fig. 7. It has been modeled in compliance with the dimensions of each element as specified by the supplier. It should also be noted that the boiling meter elements

are symmetrical concerning the heater in the middle. The handle contains the resin continuity, two Kapton layers, two adhesive layers, and an electrical link. The color legend indicating the element's boiling meter is shown at the bottom of Fig. 7.

#### 3.2. Governing equations

The following assumptions were adopted for the analysis.

- The FC-72 liquid is a Newtonian and incompressible fluid.
- The density variation of the FC-72 liquid is accounted for only in the buoyancy term of the momentum balance equation (Boussinesq approximation).
- The specific heat capacity and the thermal conductivity of the FC-72 are considered as constant over the temperature range from 20 to 45 °C, since their relative variations ( $\Delta c_{FC}/c_{FC}(T_{FC}=20^{\circ}C)$ ) and  $\Delta \lambda_{FC}/\lambda_{FC}(T_{FC}=20^{\circ}C)$ ) is low and less than 3.5 % and 5 %, respectively [36].
- Contact between FC-72 and all solid components is considered impermeable and perfect.
- Contact between solids is considered as perfect.
- The only heat source is assumed to be the heater film module in the boiling meter.
- The external walls of the cell are subject to convection with the ambient air and radiation with the outside considered at the ambient air temperature.
- The natural convection regime is considered as laminar since the Rayleigh number  $\left(Ra = \frac{g\beta_T\Delta TD^3}{\nu\chi}\right)$  does not exceed 1.5.10<sup>8</sup> for the vertical configuration, and 3.10<sup>8</sup> for the horizontal configuration
- To facilitate convergence and simulation stability, the fluid is initially assumed to be at rest, and the initial velocity is calculated iteratively in Star-CCM+.

Considering the hypotheses adopted, the model to be solved to study the phenomenon of natural convection of the FC-72 is based on the equations of continuity (Eq. (1)), momentum and heat balance (Eqs. (2) and (3)). These equations are written as follows:

$$\frac{\partial u_i}{\partial x_i} = 0 \tag{1}$$

$$\rho_{ref}\left(\frac{\partial u_i}{\partial t} + u_j \frac{\partial u_i}{\partial x_j}\right) = \frac{\partial}{\partial x_j} \left(\mu \frac{\partial u_i}{\partial x_j}\right) - \frac{\partial p}{\partial x_i} + \rho_{ref} g_i \left(1 - \beta_T \left(T_{FC} - T_{ref}\right)\right)$$
(2)

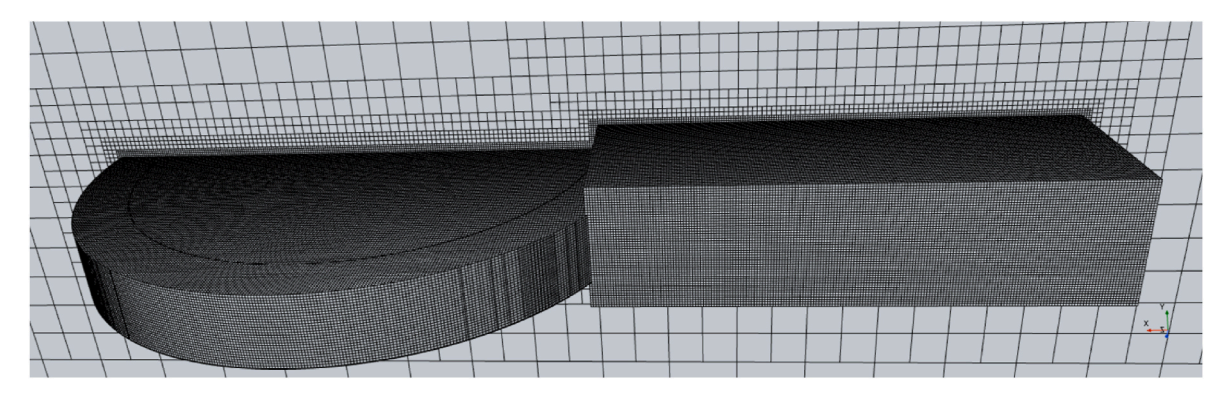


Fig. 8. Computational mesh: boiling meter and a small cross-section of the FC-72 Oxy plane counter.

**Table 3**Mesh details and parameters adopted in the vertical and horizontal configurations.

Regions	Base size	Cells number	Surface control	Target surface size	Surface growth rate
Heater film	100 μm	32115	X	30 μm	Х
Adhesive and Kapton	100 μm	94140	X	25 μm	X
Circular adhesive layers	100 μm	63352	X	25 μm	X
Copper	200 μm	147117	Contact with adhesive layers and FC-72	100 μm	slow
Heat fluxmeter	100 μm	147117	X	100 μm	X
Resin	200 μm	92299	Contact with adhesive layers and FC-72	100 μm	slow
FC-72	200 μm	961070	Thermal layer with boiling meter	100 μm	medium
Plexiglass	2 mm	153600	Contact with FC-72	200 μm	fast

$$\rho_{ref}c_{FC}\left(\frac{\partial T_{FC}}{\partial t} + u_i \frac{\partial T_{FC}}{\partial x_i}\right) = \frac{\partial}{\partial x_i} \left(\lambda_{FC} \frac{\partial T_{FC}}{\partial x_i}\right)$$
(3)

where i and j indicate the number of cartesian reference axes.  $u_i$  and/or  $u_j$ , T, and p represent, respectively, the velocity, temperature, and pressure of the fluid.  $x_i$  or  $x_j$  are the cartesian coordinates.  $\lambda_{FC}$ ,  $\mu$ , and  $c_{FC}$  are, respectively, the thermal conductivity, the dynamic viscosity, and the specific heat capacity of the liquid.  $\rho_{ref}$  and  $\beta_T$  denote, respectively, the fluid density and the thermal expansion coefficient of the fluid at the reference temperature  $T_{ref}$ .

For the momentum equations ("no slip" and "impermeable") boundary conditions are set at all solid walls:

$$\mathbf{u} = 0, \frac{\partial u_i}{\partial n} = 0 \tag{4}$$

For solid components, the equation to be solved is that of energy (Eq. (5)):

$$\rho_{s}c_{s}\frac{\partial T_{s}}{\partial t} = \frac{\partial}{\partial x_{i}}\left(\lambda_{s}\frac{\partial T_{s}}{\partial x_{i}}\right) + q \tag{5}$$

where q represents the volumetric heat source, it is considered zero for all solid components except the heater film.

The external walls of the plexiglass cell are under mixed convective and radiative conditions with ambient air at 21.5  $^{\circ}\text{C}$ :

$$-\lambda_s \frac{\partial T_s}{\partial n} = h(T_s - T_a) \tag{6}$$

where  $h=6.5~W/(m^2{}^\circ C)$ , is the heat transfer coefficient of convection and radiation between the plexiglass walls and the air. It should be noted that external air does not influence heat transfer inside the cell, due to the thermal resistance of the Plexiglass cell.

For both configurations, the initial velocity of FC-72 was assumed to be zero.

$$\mathbf{u}_{FC}(x_i, t=0) = 0 \tag{7}$$

For the vertical configuration, the initial temperatures of the fluid and all solid components are:

$$T_{FC}(x_i, t=0) = T_s(x_i, t=0) = 21.5 \,^{\circ}\text{C}$$
 (8)

Experiments in the horizontal configuration were carried out just after those performed in the vertical configuration. For this reason, the initial fluid temperature and boiling meter components are adapted for horizontal configuration to suit the experimental conditions before switching on the heater film. Thus, according to experimental temperatures, the temperature of the boiling meter components is 23  $^{\circ}$ C and the temperature of the FC-72 and the plexiglass cell is 21.8  $^{\circ}$ C.

The three-dimensional fluid dynamics (CFD) software Star CCM+ was used to solve the transport equations. This software mainly uses the finite volume method to discretize the partial differential equations (1)–(4) on a spatial mesh thanks to a first-order integration scheme in space. Time discretization is performed using a first-order implicit scheme. The solver used is the coupled flow model, whereby the continuity and momentum conservation equations are solved simultaneously as a system of vector equations. The velocity field is determined by the momentum equations, while the pressure is deduced from the continuity equation. This model is combined with the coupled energy model. The conservation equations for mass, momentum, and energy are solved thanks to a time-incremental (or pseudo-temporal) approach [29].

In the Star-CCM + code, the normalized residual is calculated using the RMS (Root Mean Squared) value of a residue calculated over all cells. This residue corresponds to the difference to 0 of the discretized equation in a cell calculated with the last value of the solution [29]. The convergence criterion requires that the normalized residuals become less than  $10^{-7}$  for the continuity and energy equations, and  $10^{-4}$  for the momentum equations. The maximum number of inner iterations for a time step has been set to 240.

#### 3.3. Domain's definitions and meshes

As indicated before, the experimental system tested in this work consists of a Plexiglass cell containing FC-72 as the working fluid, which surrounds the boiling meter. Two domains are defined: one fluid domain for the FC-72 liquid, and the solid domain includes the plexiglass cell and the boiling meter components.

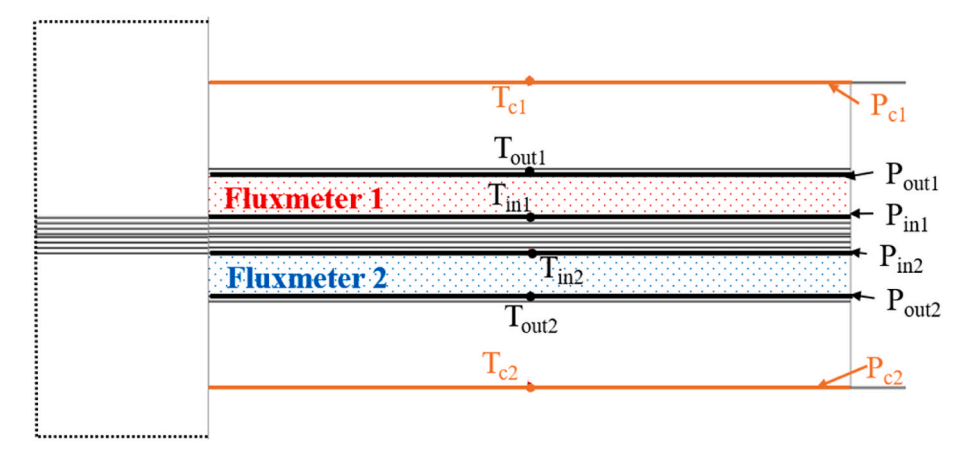


Fig. 9. Location of the points corresponding to the temperature output (T) and the surface where the heat transfer rate (P) is calculated in the boiling meter. Subscripts 'in' and 'out' indicate inner and outer points or faces, respectively, while subscript 'c' designates copper points and faces. Numbers 1 and 2 indicate component numbers.

**Table 4**Applied heat source on the boiling meter heater and associated time interval.

Imposed power	0.325 W	0.861 W	1.326 W
Interval time	[0, 90s]	[91, 190s]	[191, 280s]

Fig. 8 shows the 3D mesh of the boiling meter with a small cross-section of the FC-72 Oxy plane counter.

The heater film, adhesive layers, and Kapton layers were meshed using a trimmed mesh for both configurations. Next, the heat fluxmeters and the copper disks were meshed using the same mesh type generation but with a size and refinement adapted to the contact with the adhesive layers and the FC-72 domain. The FC-72 domain is meshed using a trimmed mesh. The surface control technique is used to adjust the mesh resolution on the specific surfaces. The aim is to increase the density of mesh elements at the interface regions (liquid/solid or solid/solid) to accurately capture geometric details and physical phenomena. The resin mesh was adjusted to ensure continuity with the boiling meter elements and the FC-72, as shown in Fig. 8. For Plexiglass, the mesh size was modified with a coarser mesh (Table 3) to minimize calculation time.

On the other hand, the heater film and the electrical link in the handle are treated as two separate parts in perfect contact to impose the heating condition on the heater film only. The surface growth rate, which measures the variation in the size of mesh elements from one surface to another, has been adapted to adjust the mesh from one component to another. In addition, mesh quality is assessed in terms of cell quality [29]. The cell quality values vary between 0.65 and 1 inside the boiling meter, between 0.8 and 1 in the interface areas between the boiling meter and the liquid, and between 0.3 and 1 in the Plexiglass.

The values of the various parameters adopted in the mesh generation for the vertical and horizontal configurations are summarized in Table 3.

It should be noted that the impact of the mesh quality and of the time step on temperatures and heat flux was evaluated in previous numerical simulations [38]. A comparison between two meshes composed respectively of 512027 and 1701154 cells has been carried out which allowed to conclude that a refined mesh, well aligned at the solid-fluid interfaces, gives more accurate results. We used similar technique of meshing like that of the second mesh used in Ref. [38], which constitutes a good compromise between accuracy and computation time. All simulations were carried out on a desktop computer equipped with an Intel® Xeon® W5-3433 @ 1.99 GHz processor, 128 GB RAM, and an NVIDIA RTX A2000 GPU with 12 GB VRAM. Estimated computing times for vertical and horizontal configurations are 12 h and 22 h respectively, using 10 processor cores.

The mesh adopted in the present work minimizes the impact of the

mesh parameters on the solution obtained. A fixed time step of 0.01s was adopted along all simulations.

### 3.4. Choice of the location of the temperatures and of the heat transfer rate extracted from the simulations

The choice of measurement points and faces for calculating temperature and heat transfer rate is based on an in-depth analysis of the experimental results. To better understand the evolution of the data obtained, we decided to analyze these measurements by post-processing the temperatures on both faces of the heat fluxmeters, as the position of the thermocouples is likely to influence the measurements of these parameters. As shown in Fig. 9, the temperature is calculated at points located at the inner ( $T_{in1}$  and  $T_{in2}$ ) and outer ( $T_{out1}$  and  $T_{out2}$ ) points on the faces of both heat fluxmeters in addition to the outer faces of the copper module ( $T_{c1}$  and  $T_{c2}$ ). The heat transfer rate is calculated by integrating the heat flux density over the inner ( $P_{in1}$  and  $P_{in2}$ ) and outer ( $P_{out1}$  and  $P_{out2}$ ) surfaces of the two heat fluxmeters, as well as the outer faces of the copper module ( $P_{c1}$  and  $P_{c2}$ ).

#### 4. Results and discussion

In the following, numerical and experimental results are presented. As we do not have access to the exact locations of the thermocouples and of the thermopile (the sensitive part of the heat fluxmeter) in the Captec sensors [24], the numerical results for heat transfer rate and temperature will be presented on the upper and lower sides of each of the heat fluxmeters. We first compare the numerical results with the experimental results in the case of a vertical configuration, and then in the horizontal configuration of the boiling meter. It should be remembered that in the vertical configuration, the heat transfers are symmetrical regarding the symmetrical plane of the boiling meter. In contrast, in the horizontal configuration, the heat transfer is asymmetrical due to a natural convection regime of the fluid on the top face and a dominant conduction regime in the fluid on the bottom face.

#### 4.1. Vertical configuration

The numerical simulations were carried out using the same protocol as that adopted for the experiment. It can be summarized as follows: starting from a uniform temperature throughout the cell, equal to the room temperature, an electrical power, dissipated in the form of heat by the Joule effect, is imposed on the boiling meter's heater for a given time interval. Once a quasi-steady state regime has been reached, further power is applied until a new one is reached again.

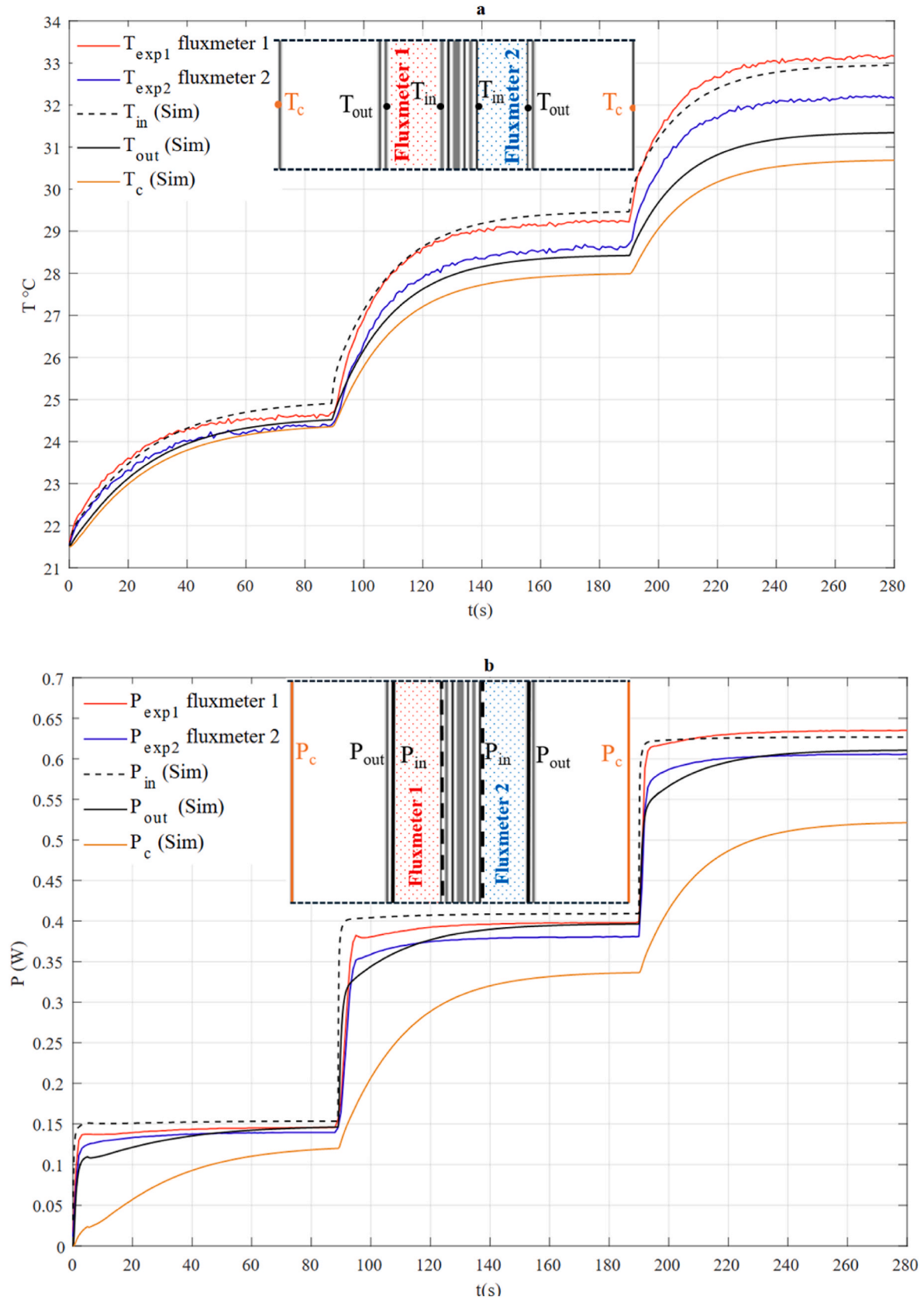


Fig. 10. Time evolution of (a) temperatures and (b) heat transfer rates calculated on the inner and outer points and faces of the heat fluxmeter, as well as on the external points and faces of the copper disc compared with the experimental data. (c) Time variation of the relative differences between measured and calculated heat transfer rates on the inner and outer faces.

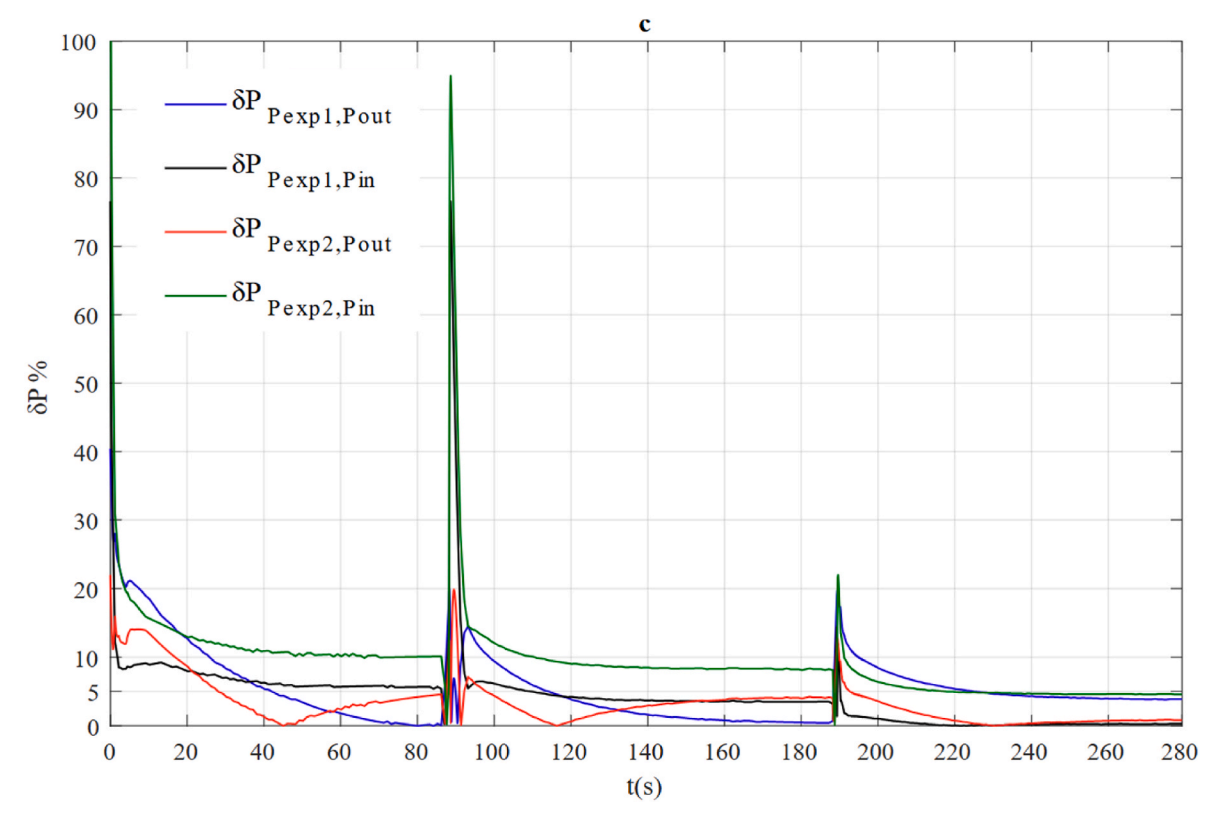


Fig. 10. (continued).

The power ratings given in Table 4 are used as input for the numerical model, as the total heat source is imposed on the heater module during the corresponding time intervals given in Table 4. These are the operating conditions used for the experiments.

Fig. 10(a) shows the temporal evolution of temperatures calculated on the inner and outer faces of the two heat fluxmeters 1 and 2, the external faces of both copper discs, and those measured by both thermocouples 1 and 2. Table 5 shows the measured and calculated heat transfer rates and temperatures values in quasi-steady state regimes for vertical configuration.

The measured temperatures  $T_{exp1}$  and  $T_{exp2}$  show the same trends as those calculated (Fig. 10(a)). However, the measured temperature  $T_{exp1}$  is close to the calculated temperature on the inner face of the fluxmeter, whatever the imposed power  $P_{imp}$ . At low power,  $T_{exp1}$  is slightly lower than  $T_{in}$  (( $T_{in} - T_{exp1}$ ) <0.3 °C). At higher power,  $T_{exp1}$  is slightly higher than  $T_{in}$  (( $T_{in} - T_{exp1}$ ) <0.2 °C). The temperature of the heat fluxmeter 2,  $T_{exp2}$ , is systematically lower than  $T_{exp1}$  and it is between the temperatures calculated at the ends of the fluxmeters.

This result shows that the calculated temperatures at the ends of the fluxmeter are well within the range of the measured temperatures ( $T_{out} < T_{exp1}, T_{exp2} < T_{in}$ ). Considering the measurement uncertainties ( $\pm 0.1\,$  °C), the observed temperature deviations can essentially be explained by the different positions of the thermocouples within the Captec fluxmeters [33]. The  $T_{in}\text{-}T_{out}$  temperature difference between the two faces of a heat fluxmeter is also significant. It reaches 1.6 °C for the highest power applied in quasi-steady state regime (Table 5). So, despite the heat fluxmeter's relatively low thickness (400  $\mu m$ ), the position of

the thermocouple can lead to significant temperature differences.

The copper temperature  $T_c$  varies similarly to that of the heat fluxmeter  $T_{out}$  at a lower temperature with a temperature difference with  $T_{out}$  which increases as the imposed power increases. This difference reaches around  $1^\circ C$  for the third power imposed ( $P_{imp}=1.326$  W). Such a difference is due to the low thermal conductivity (0.25 W/(m. $^\circ$ C)) of the adhesive layer inserted between the heat fluxmeter and the copper plate.

Fig. 10(b) shows the evolution of the heat transfer rates measured with the fluxmeters 1 and 2 ( $P_{exp1}$  and  $P_{exp2}$ ) and calculated on the inner and outer faces of the heat fluxmeter. One recall that for the symmetrical configuration, the numerical results are identical for the two heat fluxmeters. Whatever the imposed power, the evolution of the measured and calculated heat transfer rates shows similar trends. However, differences are observed between the values measured from the fluxmeters 1 and 2. These differences remain small (<5 %) and can be explained by sensor measurement uncertainties.

Fig. 10(c) shows the temporal evolution of the relative differences between measured and calculated heat transfer rates on the inner and outer faces. The relative difference between the heat transfer rate measured by the heat fluxmeter 1 and that calculated on the external face of the heat fluxmeter 1 ( $\delta P_{P_{exp}1},P_{out}=\frac{\left|P_{exp}1-P_{out}\right|}{P_{exp}1}$ ) varies between 5 % and 20 % depending on the power imposed, in the transient regime. This gap then decreases versus time, reaching almost zero values in the quasisteady state regime (Table 5 and Fig. 11), for the first two imposed powers (0.325 W and 0.861 W); while the gap remains below 5 % for the

**Table 5**Measured and calculated heat transfer rates and temperatures values in steady state regimes for the vertical configuration.

P <sub>imp</sub> (W)	T <sub>exp1</sub> (°C)	T <sub>exp2</sub> (°C)	T <sub>in</sub> (°C)	T <sub>out</sub> (°C)	T <sub>c</sub> (°C)	P <sub>exp1</sub> (W)	P <sub>exp2</sub> (W)	P <sub>in</sub> (W)	P <sub>out</sub> (W)	P <sub>c</sub> (W)
0.325	24.61	24.4	24.9	24.5	24.3	0.139	0.146	0.153	0.146	0.119
0.861	29.2	28.6	29.4	28.9	28.4	0.398	0.38	0.408	0.396	0.346
1.326	33.1	32.1	32.9	31.3	30.7	0.635	0.605	0.626	0.61	0.521

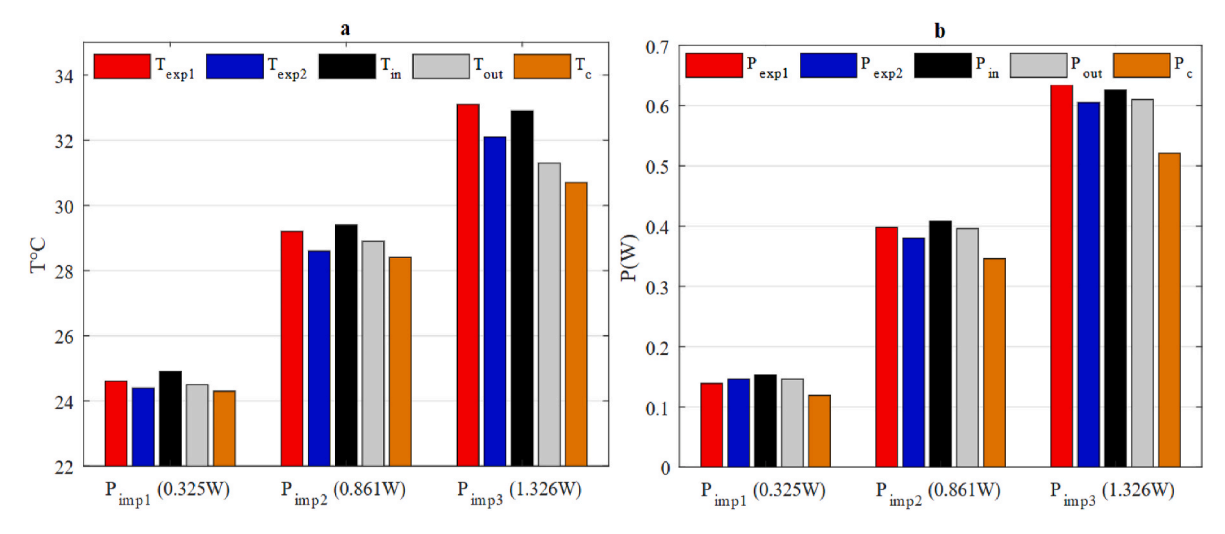


Fig. 11. Bar chart diagrams of the measured and calculated (a) temperatures and (b) heat transfer rates values in quasi-steady state regimes for the vertical configuration for the three powers imposed:  $P_{imp1} = 0.325 \text{ W}$ ,  $P_{imp2} = 0.861 \text{ W}$ ,  $P_{imp3} = 1.326 \text{ W}$ .

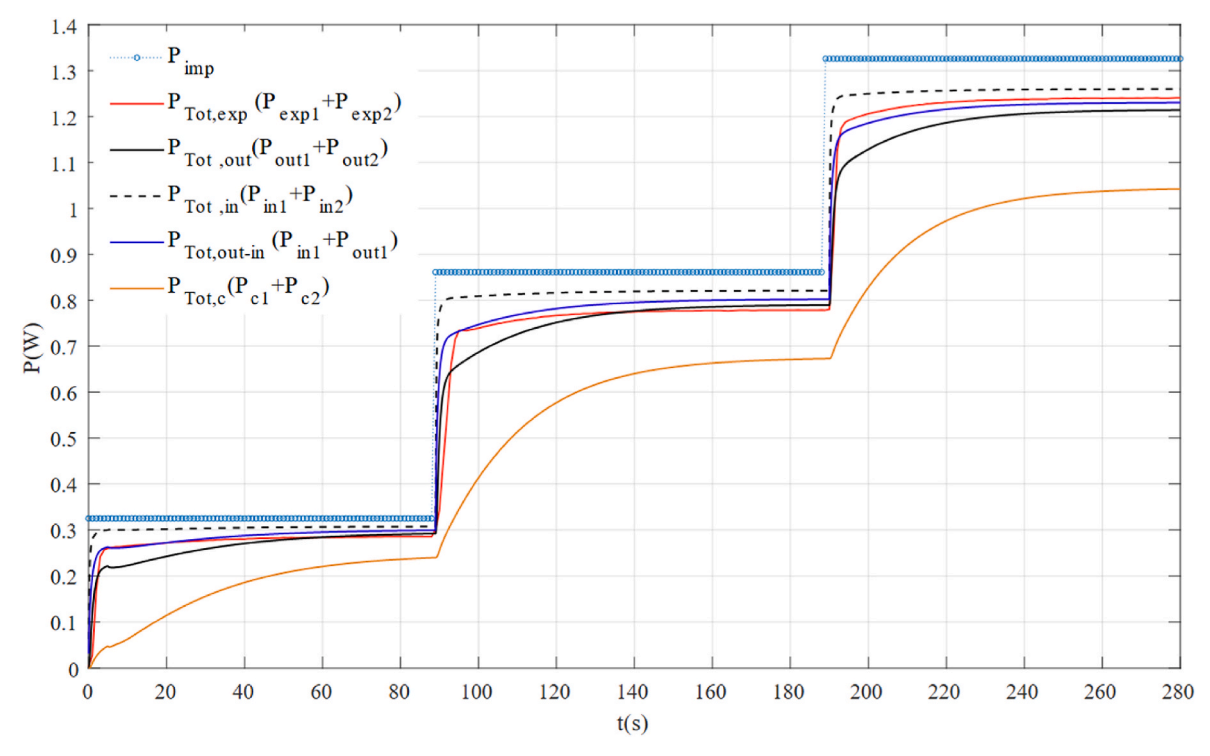


Fig. 12. Temporal evolution of the total heat transfer rate, experimental (sum of heat transfer rates measured by heat fluxmeters 1 and 2), numerical calculated on the inner faces, numerical calculated as the sum of the inner and outer heat transfer rates, numerical calculated on the faces of the copper discs, and the experimentally imposed power for vertical configuration.

last imposed power 1.326 W.

The relative difference between the measured heat transfer rate  $P_{\text{exp1}}$  and the heat transfer rate calculated on the inner face  $P_{\text{in}}$  ( $\delta P_{P_{\text{exp1}},P_{\text{in}}} = \frac{|P_{\text{exp1}}-P_{\text{in}}|}{P_{\text{exp1}}}$ ) decreases with increasing the imposed power. In the quasisteady state regime, it lies between 5 % and 10 % for the 0.325 W imposed power and decreases with the imposed power. For the imposed

Table 6
Applied heat source imposed to the boiling meter heater and associated time interval.

Imposed power (W)	0.325	1.431	2.66
Interval time (s)	[30, 208s]	[209, 395s]	[396, 540s]

power of 1.326 W, the deviation is close to zero (Table 5 and Fig. 11).

Concerning the relative deviations between the measured heat transfer rate  $P_{\text{exp1}}$  and those calculated on the inner and outer faces  $(\delta P_{P_{\text{exp2}},P_{\text{out}}} = \frac{|P_{\text{exp2}} - P_{\text{out}}|}{P_{\text{exp1}}})$  and  $\delta P_{P_{\text{exp1}},P_{\text{in}}} = \frac{|P_{\text{exp2}} - P_{\text{in}}|}{P_{\text{exp2}}})$ , we observe that the deviation  $(\delta P_{P_{\text{exp2}},P_{\text{out}}})$  is always smaller than the second one  $(\delta P_{P_{\text{exp1}},P_{\text{in}}})$  whatever the imposed power. In the quasi-steady state regime, this deviation varies between 0 % and 5 % for the two first imposed powers and becomes virtually zero for the third power (Table 5 and Fig. 11).

However, these deviations are much more pronounced at the start of each power change period. On one hand, this is because the heat fluxmeters are assumed to be homogeneous, whereas in fact they are made of multilayer materials. On the other hand, it is because the sensitive parts of the heat fluxmeters are not located at the same distance from the

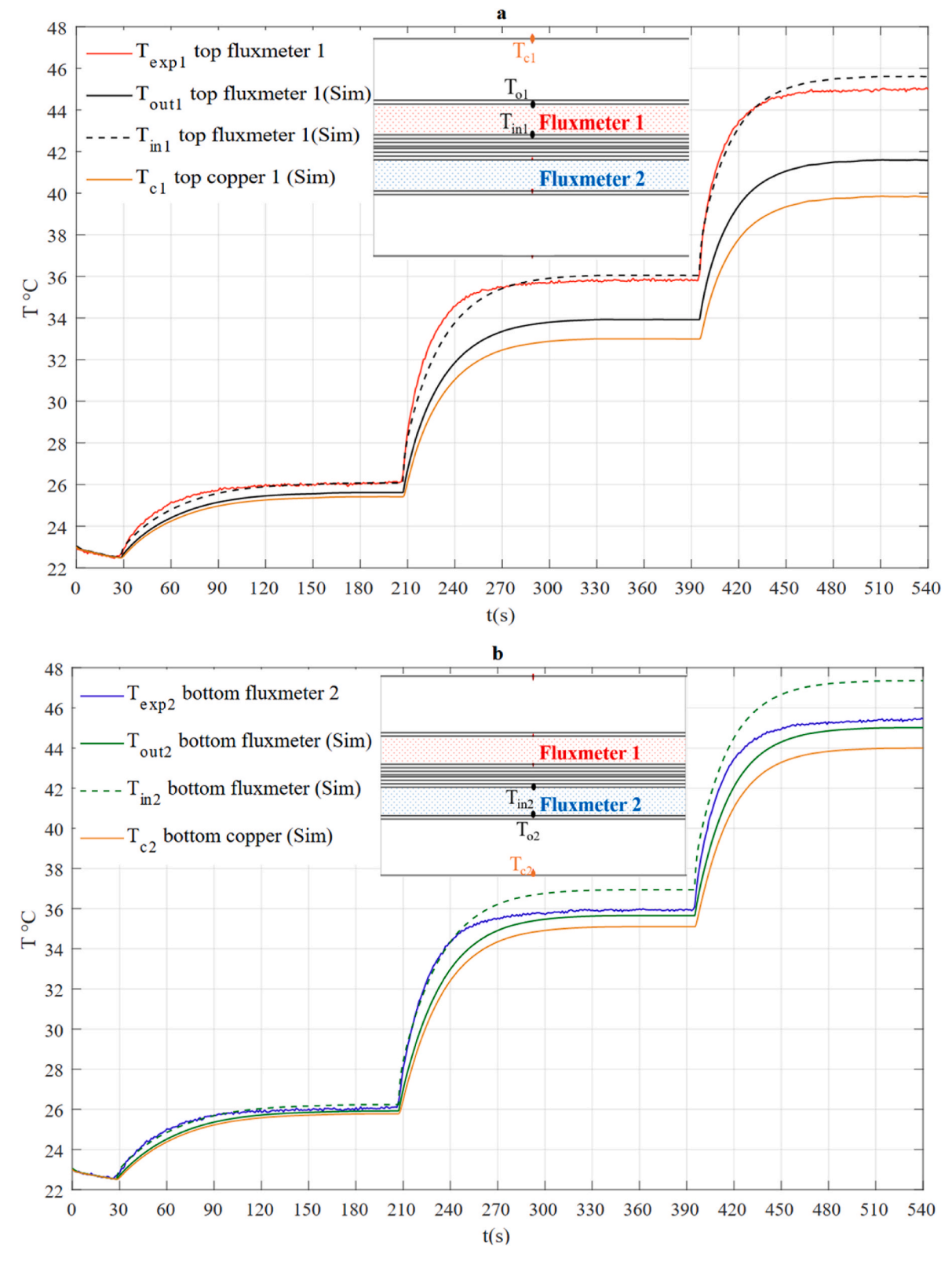


Fig. 13. Time evolution (a) and (b) of the calculated temperatures at the inner and outer points of both heat fluxmeters and the outer points of the copper disks, compared with the experimental temperature. (c) and (d) Time evolution of the calculated heat transfer rates on the inner and outer faces of both heat fluxmeters and at the faces of the copper disks, compared with the heat transfer rate measured by both heat fluxmeters 1 and 2. (e) Temporal variation in relative differences between measured and calculated heat transfer rates on inner and outer surfaces.

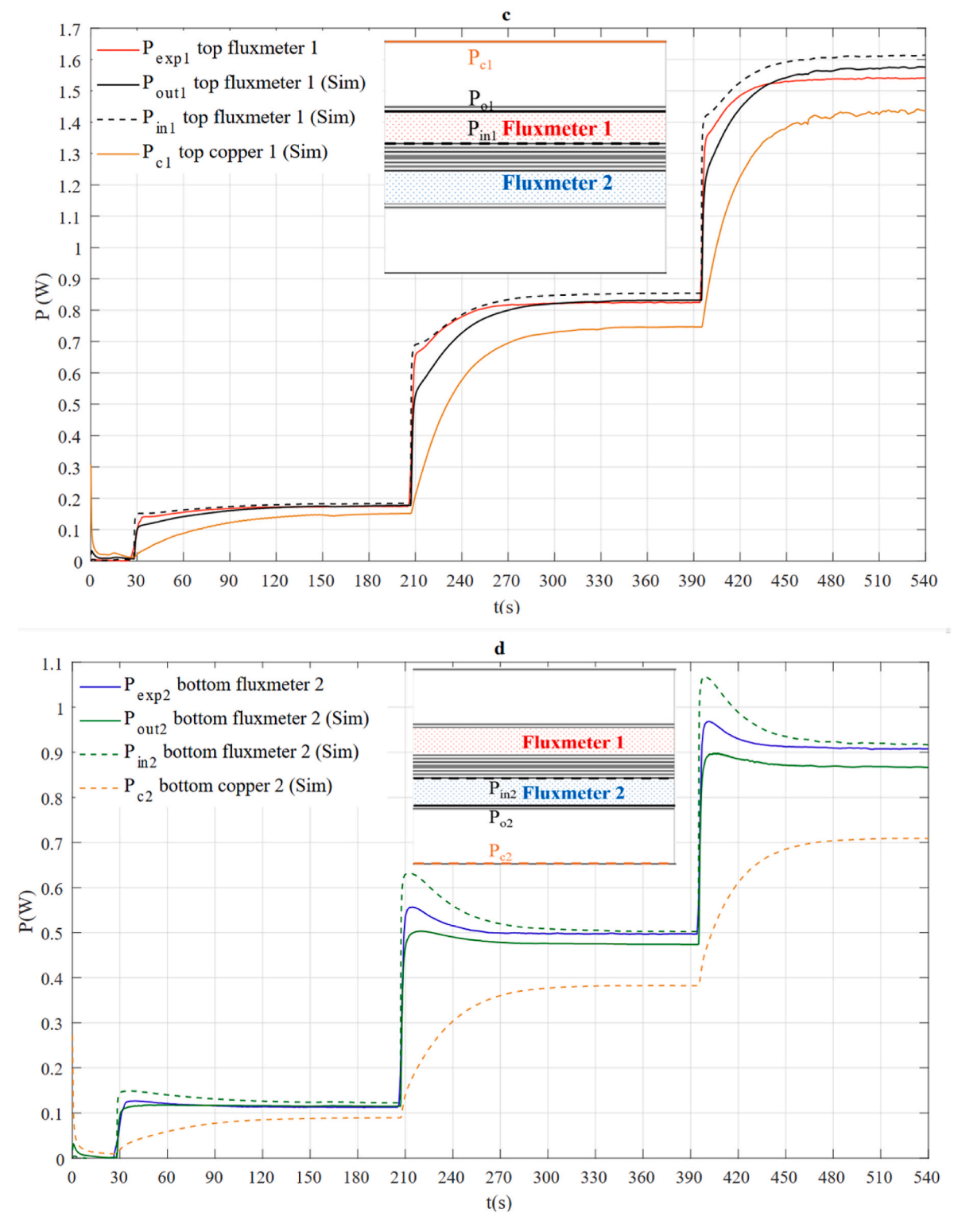


Fig. 13. (continued).

plane of symmetry of the boiling meter.

In addition to these observations, the heat transfer rate calculated on the inner face is systematically higher than that calculated on the outer face of the heat fluxmeter, for all the imposed powers. This difference is due to the lateral heat losses by the lateral side of the heat fluxmeters.

A significant difference between the heat transfer rate calculated on the faces of the copper discs and those calculated on the outer faces of heat fluxmeters 1 and 2 can be observed in Fig. 10(b). The largest differences are observed at the beginning of a newly imposed power value period. At the beginning of a new period, the time evolution of the heat transfer rate on the faces of the copper discs is driven by the accumulation of heat inside the copper discs. As the heat capacity of the copper discs is not negligible, it explains why the heat transfer rate at the surface of the copper discs  $P_c$  is significantly lower than that at the outer faces of the heat fluxmeters. At times close to the quasi-steady state regime, differences remain. These differences are due to the lateral heat

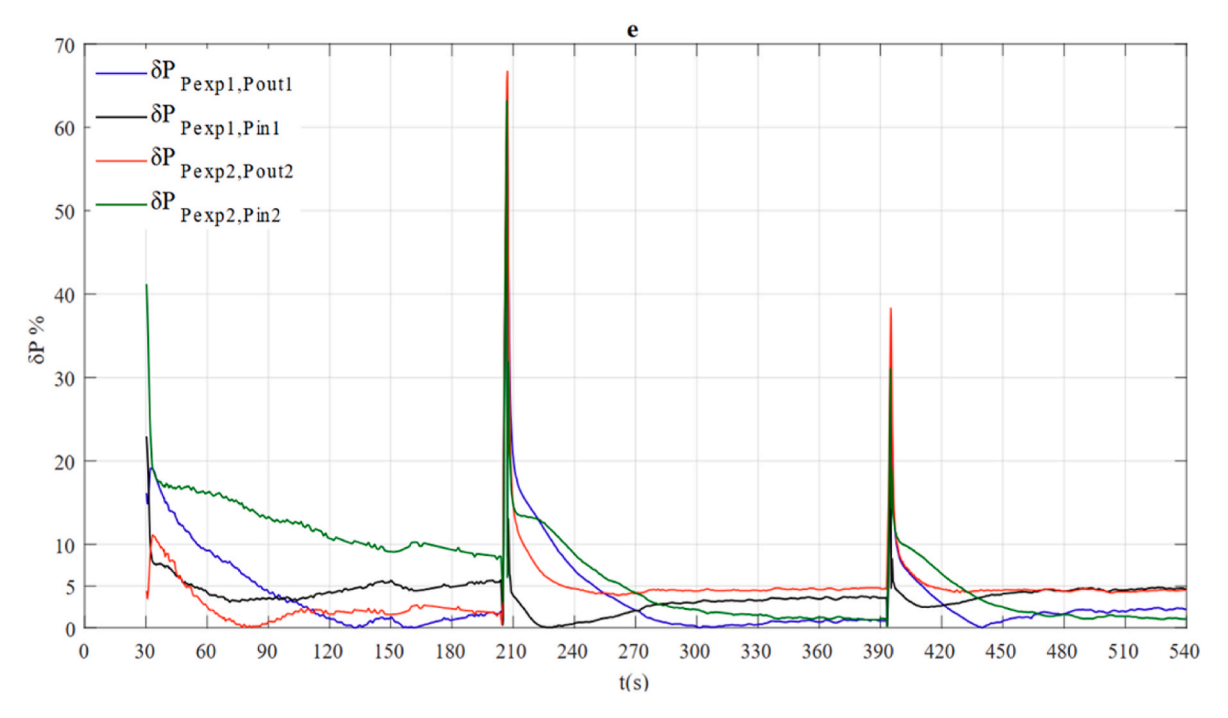


Fig. 13. (continued).

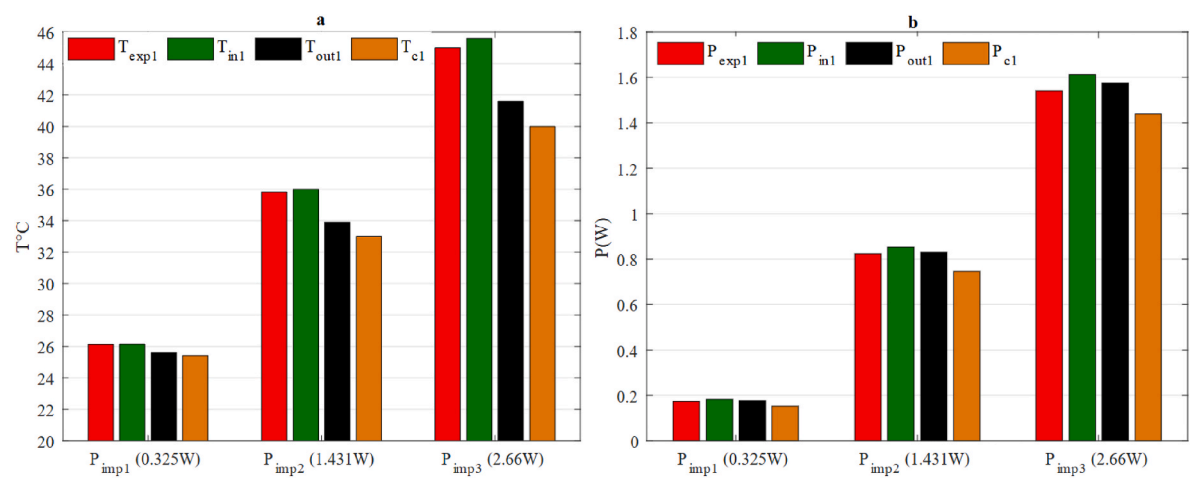


Fig. 14. Bar chart diagrams of the measured and calculated (a) temperatures and (b) heat transfer rates values in quasi-steady state regimes on the top side for the horizontal configuration for the three powers imposed:  $P_{imp1} = 0.325 \text{ W}$ ,  $P_{imp2} = 1.431 \text{ W}$ ,  $P_{imp3} = 2.66 \text{ W}$ .

losses from the lateral side of the copper discs. They can exceed 20 % depending on the imposed power.

Fig. 12 shows the total heat transfer rate measured  $(P_{Tot,exp} = P_{exp1} + P_{exp2})$  and calculated on the inner  $(P_{Tot, in} = P_{in1} + P_{in2})$  and outer faces  $(P_{Tot,out} = P_{out1} + P_{out2})$  of the heat fluxmeters; the sum of the inner and outer heat transfer rates  $(P_{in1} + P_{out1})$ ; the sum of the heat transfer rates calculated on the copper faces  $(P_{c1} + P_{c2})$ , and the imposed power. The measured total heat transfer rate  $P_{Tot, exp}$  ranges in between the two total heat transfer rates calculated on the inner faces  $P_{Tot,in}$  and the outer faces  $P_{Tot,out}$  of the heat fluxmeters, especially in the first few moments when a new heat power is applied. It is interesting to observe that  $P_{Tot, exp}$  is closer to  $P_{Tot,out-in}$  than  $P_{Tot,in}$  or  $P_{Tot,out}$ . This is because one of the two measured heat transfer rates is close to that calculated on the inner face, and the other is close to that calculated on the outer face, as discussed previously.

From these results, it is essential to note that the imposed power  $(P_{imp})$  is higher than the total measured and calculated heat transfer

rate. This difference is due to the accumulation of heat in the different parts of the boiling meter during the transient period and to the lateral heat loss acting all through the period of heating. Notably due to these lateral heat losses, one can see in Fig. 12 that the total heat transfer rate at the surfaces of the copper discs is always significantly lower than the imposed power. In the quasi-steady state regime, this difference increases with the amount of the imposed power reaching 25 % for the highest value of the imposed power.

In summary, the asymmetry of temperatures and heat fluxes measured at the heat fluxmeter level can be explained by the poorly controlled positioning of thermocouples and thermopiles in heat fluxmeters, despite the small spatial scales considered (a few tens of  $\mu$ m). These results show that the inertia of the boiling meter's constituent materials and lateral losses influence the results. All these parameters need to be considered in the design of the boiling meter sensor to accurately assess heat transfer to the walls of the boiling meter in contact with the liquid. Numerical simulation showed that heat fluxmeter 1 gave

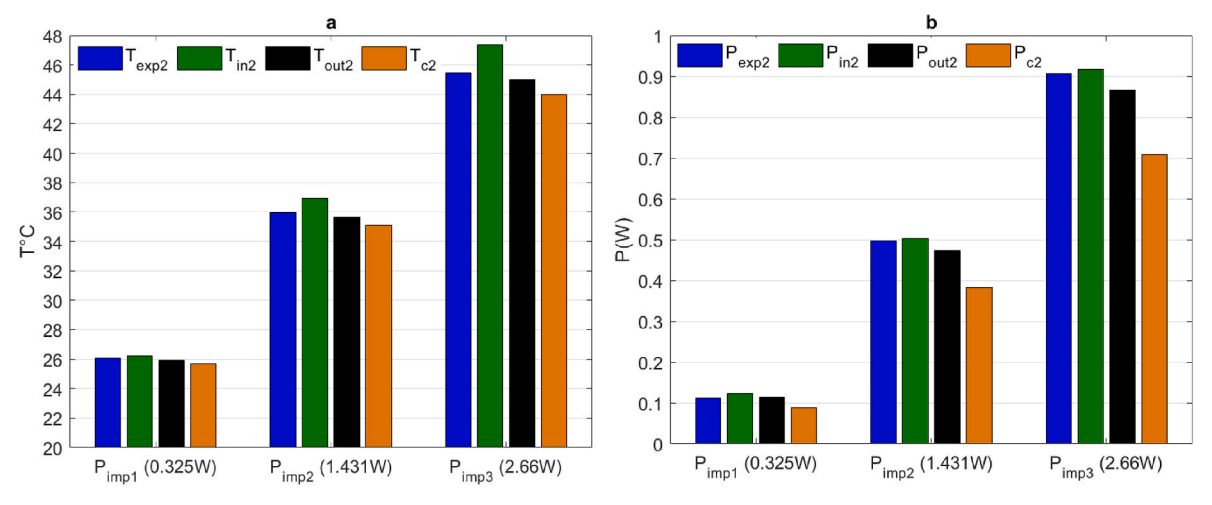


Fig. 15. Bar chart diagrams of the measured and calculated temperatures (a) and heat transfer rates (b) values in quasi-steady state regimes on the bottom side for the horizontal configuration for the three powers imposed:  $P_{imp1} = 0.325 \text{ W}$ ,  $P_{imp2} = 1.431 \text{ W}$ ,  $P_{imp3} = 2.66 \text{ W}$ .

 Table 7

 Measured and calculated heat transfer rates and temperatures values in quasi-steady state regimes on the top side for the horizontal configuration.

P <sub>imp</sub> (W)	$T_{exp1}$ (°C)	T <sub>in1</sub> (°C)	T <sub>out1</sub> (°C)	T <sub>c1</sub> (°C)	P <sub>exp1</sub> (W)	P <sub>in1</sub> (W)	P <sub>out1</sub> (W)	P <sub>c1</sub> (W)
0.325	26.13	26.14	25.61	25.41	0.174	0.183	0.177	0.152
1.431	35.81	36	33.9	33	0.823	0.853	0.831	0.746
2.66	45	45.6	41.6	40	1.54	1.613	1.575	1.44

 Table 8

 Measured and calculated heat transfer rates and temperatures values on the bottom side in quasi-steady state regimes for the horizontal configuration.

P <sub>imp</sub> (W)	$T_{exp2}$ (°C)	$T_{in2}$ (°C)	T <sub>out2</sub> (°C)	T <sub>c2</sub> (°C)	P <sub>exp2</sub> (W)	P <sub>in2</sub> (W)	P <sub>out2</sub> (W)	P <sub>c2</sub> (W)
0.325	26.1	26.23	25.91	25.87	0.112	0.122	0.114	0.089
1.431	35.95	36.93	35.65	35.09	0.497	0.502	0.473	0.383
2.66	45.44	47.35	45.01	44	0.907	0.918	0.867	0.709

a heat transfer rate value ( $P_{exp1}$ ) close to that calculated on the inner face of the heat fluxmeter  $P_{in}$ , while fluxmeter 2 gave a heat transfer rate value  $P_{exp2}$  close to that calculated on the outer face  $P_{out}$ .

#### 4.2. Horizontal configuration

For this configuration, the powers imposed on the heater and the associated time intervals are reported in Table 6.

In this configuration, the heat transfer is asymmetrical in relation to the heat source placed in the center of the boiling meter and the orientation of the boiling meter with gravity.

Table 7, Fig. 14, Table 8, and Fig. 15 show the measured and calculated temperatures and heat transfer rates values in steady state regimes for the horizontal configuration at the top and bottom sides, respectively.

In Fig. 13(a) and (b), the curves  $T_{in2}$  and  $T_{out2}$  represent the time evolution of the temperatures calculated at the inner and outer faces of the bottom heat fluxmeter 2. The highest temperature is on the face close to the heating element  $T_{in2}$ . Whatever the power level,  $T_{exp2}$  lies between the two calculated temperatures  $T_{in2}$  and  $T_{out2}$ .

For the top heat fluxmeter 1 (Fig. 13(a)), the differences between  $T_{in1}$  and  $T_{out1}$  temperatures are small for the low imposed power ( $P_{imp} = 0.325$  W). At higher imposed power, these differences become more pronounced. For the imposed power  $P_{imp} = 2.66$  W, the difference reaches 4 °C in the quasi-steady state regime as shown in Table 7 and Fig. 14. The measured temperature  $T_{exp1}$  is in between those calculated at the ends of the heat fluxmeter 1 ( $T_{in1}$  and  $T_{out1}$ ), except for the transient regime at intermediate power ( $P_{imp} = 1.431$  W). However, this

 $T_{exp1}$  temperature remains very close to the calculated  $T_{in1}$  temperature. As previously observed in vertical configuration, the  $T_{exp1}$  thermocouple is close to the inner wall temperature of the heat fluxmeter  $(T_{in1})$ .

The temperatures measured are like those calculated on the inner faces of both heat fluxmeters in the transient regime. However, in the quasi-steady state regime, the temperature measured by the thermocouple 1 Texp1 corresponds more closely to the temperature calculated at the inner face of the heat fluxmeter 1 Tin1, with a maximum difference of 0.6 °C for the highest imposed power in steady state regime (Table 7 and Fig. 14). By contrast, the temperature measured by the thermocouple 2  $T_{exp2}$  is closer to that calculated at the outer face of heat fluxmeter 2 T<sub>out2</sub>, as shown in Figs. 13(b), and Fig. 15. The highest difference does not exceed 0.4 °C for the imposed power equal to 2.66 W in steady state regime. Then the simulation results lead to the conclusion that T<sub>exp1</sub> is close to T<sub>in1</sub> and T<sub>exp2</sub> is close to T<sub>out2</sub>. Which in other words means that the location of the thermocouples is not identical in the two heat fluxmeters. Due to the low thermal conductivity of the heat fluxmeter as demonstrated by the numerical simulation, a significant temperature difference of a few degrees develops inside the heat fluxmeter for the highest heat power applied. Thus, the similar values of the temperatures measured by the two thermocouples Texp1 and Texp2 despite the asymmetry of the heat transfer can be explained by the difference of the location of these thermocouples.

The temperatures calculated on the copper faces  $T_{c1}$ ,  $T_{c2}$  evolve similarly to those calculated on the external faces  $T_{out1}$ ,  $T_{out2}$  of the heat fluxmeters. Nevertheless, the temperature difference is a function of the imposed power. For  $P_{imp} = 2.66$  W, in the quasi-steady state regime, this difference may reach 2 °C between the top faces and 1.7 °C between the

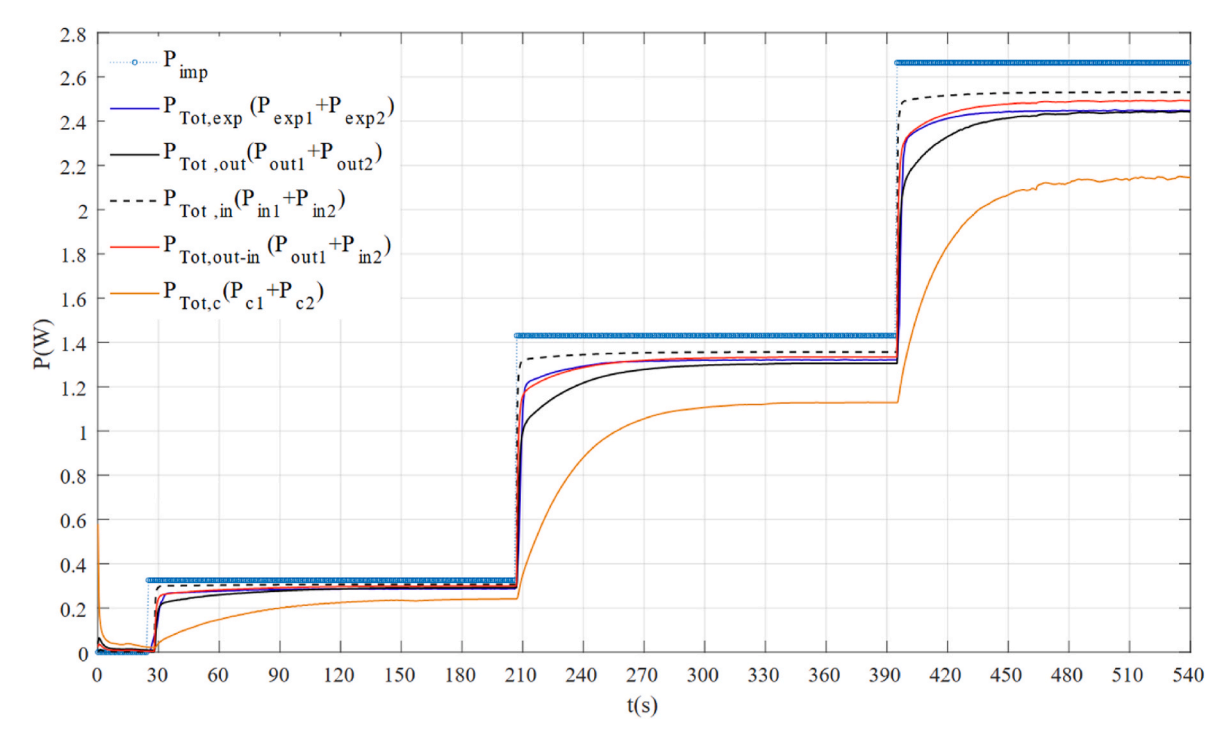


**Fig. 16.** Time evolution of the total heat transfer rate  $P_{Tot, exp}$  sum of the heat transfer rat measured by the top and bottom heat fluxmeters),  $P_{Tot, in}$  sum of the calculated heat transfer rate on the inner faces of the heat fluxmeters,  $P_{Tot, out}$  sum of the calculated heat transfer rate on the outer faces of the heat fluxmeters,  $P_{Tot, out}$  sum of the calculated heat transfer rate as the sum of the heat transfer rate on the inner face of the heat fluxmeter 1 and the heat transfer rate at the outer face of the heat fluxmeter 2,  $P_{Tot, c}$  sum of the calculated heat transfer rate on the outer faces of the two copper discs, and the experimentally imposed power.

bottom faces (Table 7, Fig. 14, Table 8, and Fig. 15). Again, like for the previous configuration; the observed differences are due to the adhesive layer between both modules (heat fluxmeter and copper) and copper thermal inertia.

It is worth noting that the difference between the temperature measured by the thermocouple 1  $T_{exp1}$  and that calculated on the upper copper face  $T_{c1}$  (top interface between the boiling meter and FC-72 liquid) exceeds 5 °C for the highest imposed power of 2.66 W in steady state regime (Table 7 and Fig. 14). This is an important result for the design of the boiling meter. Indeed, even if the thermocouple placed inside the heat fluxmeter 1 would have been close to its outer face, the access to the temperature at the top face of the copper disc from the knowledge of a temperature in the heat fluxmeter needs a calibration. Such a calibration can be done only by knowing accurately the location of the thermocouple.

For the measured and calculated heat transfer rates (Fig. 13(c) and (d)) we observe the same trends as for the vertical configuration. The measured values of the heat fluxmeters 1 and 2 stay in between  $P_{out}$  and  $P_{in}$  calculated for the corresponding heat fluxmeter. Except for the 2.66 W power where the measured heat transfer rate at the heat fluxmeter 1 is slightly lower than the calculated heat transfer rate  $P_{out1}$  (( $P_{out1}$ - $P_{exp1}$ )/  $P_{exp1}$ <2.5 %) however this difference remains lower than the measurement error.

Fig. 13(e) shows the time evolution of the relative deviations between the measured and calculated heat transfer rates on the inner and outer faces of each fluxmeter. In the transient regime of each imposed power, the relative deviation between the measured heat transfer rate  $P_{\text{exp1}}$  and that calculated on the external face  $P_{\text{out1}}$  ( $\delta P_{P_{exp1},P_{out1}} = \frac{\left|P_{exp1}-P_{out1}\right|}{P_{exp1}}$ ), is greater than the deviation between the same measured heat transfer rate and that calculated on the inner face ( $\delta P_{P_{exp1},P_{out1}} = \frac{\left|P_{exp1}-P_{out1}\right|}{P_{exp1}}$ ). By contrast, at quasi-steady state regime, the deviation ( $\delta P_{P_{exp1},P_{out1}}$ ) becomes less than  $\delta P_{P_{exp1},P_{int1}}$  and does not exceed 5 % (Table 7 and Fig. 14).

For the bottom fluxmeter, the relative deviation  $\delta P_{P_{exp\ 2},P_{out2}}$  ( $\delta P_{P_{exp\ 2},P_{out2}} = \frac{\left|P_{exp\ 2}-P_{out2}\right|}{P_{exp\ 2}}$ ) is less than  $\delta P_{P_{exp\ 2},P_{in2}}$  ( $\delta P_{P_{exp\ 2},P_{in2}} = \frac{\left|P_{exp\ 2}-P_{in2}\right|}{P_{exp\ 2}}$ ) for an imposed power of 0.325 W and does not exceed 3 % at quasisteady state regime. For the two imposed powers of 1.431 and 2.664 W, the relative deviation ( $\delta P_{P_{exp\ 2},P_{in2}}$ ) becomes less than the external one ( $\delta P_{P_{exp\ 2},P_{out2}}$ ) and remains below 2 % at quasi-steady state regime (Table 8 and Fig. 15).

The heat transfer rate calculated on the surface of the top copper disc evolves very differently from that measured or calculated on heat fluxmeter 1. The difference between them increases with each rise in the imposed power. As already discussed for the vertical configuration, this difference is due to the accumulation of heat in the copper disc at the beginning of each period, as well as lateral heat losses at the edges of the copper disc.

On the other hand, the heat transfer rate calculated on the bottom face of the copper disc ( $P_{c2}$ ) evolves differently from that calculated on the heat fluxmeter ( $P_{out2}$ ), especially during the transient regime, where a significant difference is observed. This discrepancy increases with each rise in the imposed power. The accumulation of heat in the copper disc is a key factor contributing to this. Additionally, the observed difference is attributed to lateral losses at the edges of the copper discs, whose thickness is twice that of the heat fluxmeter.

Fig. 16 shows the total measured ( $P_{Tot, exp} = P_{exp1} + P_{exp2}$ ) and the calculated heat transfer rates on the inner and outer faces of heat fluxmeters 1 and 2 ( $P_{Tot, in} = P_{in1} + P_{in2}$  and  $P_{Tot, out} = P_{out1} + P_{out2}$ ), the sum of heat transfer rates on the outer face of heat fluxmeter 1 and the inner face of heat fluxmeter 2 ( $P_{Tot,in-out} = P_{out1} + P_{in2}$ ), the sum of heat transfer rates on the copper faces ( $P_{Tot,c} = P_{c1} + P_{c2}$ ), and the imposed power ( $P_{imp}$ ).

The total experimental heat transfer rate  $P_{Tot,\ exp}$  ranges between the total heat transfer rate calculated on the inner and outer faces  $P_{Tot,\ in}$  and  $P_{Tot,\ out}$ .

Moreover, as in the case of the vertical configuration, the total measured heat transfer rate  $P_{\text{Tot, exp}}$  is almost identical to the sum of the

heat transfer rates calculated on the outer face of heat fluxmeter 1 and that calculated on the inner face of heat fluxmeter 2 ( $P_{Tot}$ , out-in =  $P_{out1}+P_{in2}$ ) particularly for the first two power ratings. For the third power ( $P_{imp}=2.66$  W), the two curves diverge slightly due to the difference between calculated and measured heat transfer rates, observed in Fig. 13(b) for this same power.

#### 5. Conclusion and perspectives

We have developed a combined experiment-modeling approach to calibrate a boiling meter designed to analyze heat transfer between a wall and a fluid where different phenomena can develop for several operating conditions (conduction, natural convection, boiling, etc.).

Experimental results highlighted inconsistencies that had been analyzed to improve the boiling meter's performance and accurately determine the temperature and heat transfer rate at the surface of the boiling meter in contact with the fluid. To do this, we modeled and simulated the heat and momentum transfer of the whole experimental set-up comprising the cell walls, the liquid FC-72, and the boiling meter. This enabled us to interpret the experimental results and better understand the phenomena involved. Thanks to this approach, we have shown that the thermal characteristics at the wall differ significantly from those measured with heat fluxmeters.

The comparison of the numerical and experimental results showed that the experimental values for temperature and heat transfer rate at both heat fluxmeters were framed by the values calculated on both sides of the heat fluxmeters. In addition, the heat transfer rate and temperature measured at heat fluxmeter1 were closer to the values of temperature and heat transfer rate calculated on its inner face. For heat fluxmeter 2, the measured temperature is closer to that calculated on the outer face. In this way, it is possible to know accurately what the measured values correspond and to interpret the apparent inconsistencies observed in the experimental results.

Analysis of the simulation results showed that heat transfer rate and temperature vary considerably between the two sides of the same heat fluxmeter, despite its very low thickness. This is due to the heat fluxmeter's low thermal conductivity, transient heat accumulation, and lateral losses in the heat fluxmeter. Although the thicknesses involved in heat fluxmeters are only a few dozen of microns, heat transfer quantification at the boiling meter must be carried out at micron scales to control heat transfer in this sensor. This approach makes the measurement technique robust and reliable. Ultimately, it enables precise analysis of fluid-wall heat transfer using the boiling meter.

Numerical simulation has highlighted that, despite the boiling meter's low thicknesses with temperature and flux sensors close to the wall ( $\approx 1\,$  mm), heat transfer measurements at the wall are not directly accessible.

This work has led us to pursue the combined approach used to accurately determine the heat transfer laws between a fluid and a wall. Numerical simulation will be used to design a boiling meter providing more appropriate instrumentation for measuring heat transfer at a wall in contact with a fluid.

#### CRediT authorship contribution statement

Abdelkabir Zaite: Writing – review & editing, Writing – original draft, Visualization, Validation, Software, Formal analysis. Himanshi Kharkwal: Investigation. Hervé Combeau: Writing – review & editing, Writing – original draft, Supervision. Lounès Tadrist: Writing – review & editing, Writing – original draft, Supervision, Conceptualization.

#### Declaration of competing interest

The authors declare that they have no known competing financial interests or personal relationships that could have appeared to influence the work reported in this paper.

#### Acknowledgment

The authors acknowledge Ass. Prof. Ahmed Kaiss (IUSTI-AMU), Ass Prof. Magali Barthes (FEMTO-UBFC) and Prof François Lanzetta (FEMTO-UBFC). LT acknowledges the CNES (National Centre for Space Studies) for its financial support of the project ERAMEN. He also acknowledges ANR – FRANCE (French National Research Agency) for its financial support of the TraThI project ANR-21-CE50-0009-01.

#### Data availability

No data was used for the research described in the article.

#### References

- L. Léal, et al., An overview of heat transfer enhancement methods and new perspectives: focus on active methods using electroactive materials, Int. J. Heat Mass Tran. 61 (1) (2013) 505–524, https://doi.org/10.1016/j. ijheatmasstransfer.2013.01.083.
- [2] A.E. Bergles, Recent developments in enhanced heat transfer, Heat Mass Tran. 47 (8) (2011) 1001–1008.
- [3] S. Nukiyama, The maximum and minimum values of the heat Q transmitted from metal to boiling water under atmospheric pressure, Int. J. Heat Mass Tran. 9 (12) (1966) 1419–1433.
- [4] M. Stephan, K. Abdelsalam, Heat-transfer correlations for natural convection boiling, Int. J. Heat Mass Tran. 23 (1) (1980) 73–87.
- [5] S. Nishikawa, K, Y. Fujita, H. Ohta, Hidaka, Effect of the surface roughness on the nucleate boiling heat transfer over the wide range of pressure, in: In International Heat Transfer Conference Digital Library, Begel House Inc., 1982.
- [6] C.-Y. Wang, W.-T. Ji, C.-Y. Zhao, L. Chen, W.-Q. Tao, Experimental determination of the role of roughness and wettability on pool-boiling heat transfer of refrigerant, Int. J. Refrig. 153 (Sep. 2023) 205–221, https://doi.org/10.1016/j. ijrefrig.2023.06.014.
- [7] X. Yuan, Y. Du, C. Wang, Experimental study on pool boiling enhancement by unique designing of porous media with a wettability gradient, Appl. Therm. Eng. 231 (Aug. 2023) 120893, https://doi.org/10.1016/j. applthermaleng.2023.120893.
- [8] M. Volle F, M. Gradeck, D. Maillet, A. Kouachi, Lebouché, Inverse heat conduction applied to the measurement of heat fluxes on a rotating cylinder: comparison between an analytical and a numerical technique, ASME, J. Heat Transf. 130 (8) (2008), https://doi.org/10.1115/1.2928013 [Online]. Available:.
- [9] F. Volle, D. Maillet, M. Gradeck, A. Kouachi, M. Lebouché, Practical application of inverse heat conduction for wall condition estimation on a rotating cylinder, Int. J. Heat Mass Tran. 52 (1–2) (2009) 210–221, https://doi.org/10.1016/j. iiheatmasstransfer,2008.05.025.
- [10] G.M. Carlomagno, A. Ianiro, Thermo-fluid-dynamics of submerged jets impinging at short nozzle-to-plate distance: a review, Exp. Therm. Fluid Sci. 58 (2014) 15–35, https://doi.org/10.1016/j.expthermflusci.2014.06.010.
- [11] M. Može, A. Hadžić, M. Zupančič, I. Golobič, Boiling heat transfer enhancement on titanium through nucleation-promoting morphology and tailored wettability, Int. J. Heat Mass Tran. 195 (Oct. 2022) 123161, https://doi.org/10.1016/j. iiheatmasstransfer.2022.123161.
- [12] Y. Xia, R. Li, X. Gao, R. Li, Pool boiling on a biphilic surface where bubbles can move horizontally on the surface, Int. J. Heat Mass Tran. 215 (Nov. 2023) 124540, https://doi.org/10.1016/j.ijheatmasstransfer.2023.124540.
- [13] V. Scheiff, F. Bergame, J. Sebilleau, P. Ruyer, C. Colin, Experimental study of steady and transient subcooled flow boiling, Int. J. Heat Mass Tran. 164 (2021) 120548, https://doi.org/10.1016/j.ijheatmasstransfer.2020.120548.
- [14] A. Sielaff, et al., The multiscale boiling investigation on-board the International Space Station: an overview, Appl. Therm. Eng. 205 (2022) 117932, https://doi. org/10.1016/j.applthermaleng.2021.117932.
- [15] H. Huang, Y. Yang, Y. Zhu, Accurate 4D thermal imaging of uneven surfaces: theory and experiments, Int. J. Heat Mass Tran. 216 (Dec. 2023) 124580, https://doi.org/10.1016/j.ijheatmasstransfer.2023.124580.
- [16] P.R. Muniz, S.P.N. Cani, R. da S. Magalhaes, Influence of field of view of thermal imagers and angle of view on temperature measurements by infrared thermovision, IEEE Sens. J. 14 (3) (Mar. 2014) 729–733, https://doi.org/10.1109/ JSEN.2013.2287003.
- [17] N.P. Avdelidis, A. Moropoulou, Emissivity considerations in building thermography, Energy Build. 35 (7) (Aug. 2003) 663–667, https://doi.org/ 10.1016/S0378-7788(02)00210-4.
- [18] C. Meola, G.M. Carlomagno, Application of infrared thermography to adhesion science, J. Adhes. Sci. Technol. 20 (7) (Jan. 2006) 589–632, https://doi.org/ 10.1163/156856106777412491.
- [19] J. Kočí, R. Černý, A design of a semi-virtual calibration experiment for a sensitivity enhancement of general-purpose heat flow meters applied in residential buildings, Energy 261 (Dec. 2022) 125287, https://doi.org/10.1016/j.energy.2022.125287.
- [20] G. Xu, Y. Huang, B. Dong, Y. Quan, Q. Yin, J. Chai, Design and performance evaluation of a novel thin-film heat flux sensor, Case Stud. Therm. Eng. 47 (Jul. 2023) 103121, https://doi.org/10.1016/j.csite.2023.103121.
- [21] T. P, Fluxmètres thermiques, Techniques de l'ingénieur, R2900, 1988.

- [22] G. Xu, Y. Huang, Y. Quan, Q. Yin, J. Chai, J. Liu, Effect of thin-film sensors on local heat transfer in convective heat flux measurement, Case Stud. Therm. Eng. 49 (Sep. 2023) 103189, https://doi.org/10.1016/j.csite.2023.103189.
- [23] G. Cortellessa, L. Iacomini, A novel calibration system for heat flow meters: experimental and numerical analysis, Meas. J. Int. Meas. Confed. 144 (2019) 105–117, https://doi.org/10.1016/j.measurement.2019.05.053.
- [24] F. Arpino, M. Dell'Isola, G. Ficco, L. Iacomini, V. Fernicola, Design of a calibration system for heat flux meters, Int. J. Thermophys. 32 (11–12) (2011) 2727–2734, https://doi.org/10.1007/s10765-011-1054-3.
- [25] G. Cortellessa, et al., Experimental and numerical analysis in heat flow sensors calibration, J. Therm. Anal. Calorim. 138 (4) (2019) 2901–2912, https://doi.org/ 10.1007/s10973-019-08321-6.
- [26] M.N. Polyashchenkova, M.A. Chebanov, O.V. Lobach, Technological factors having effect on calibration of beam heat flux sensor, 12th Int. Conf. Semin. Micro/ Nanotechnol. Elect. Devices 4 (2) (2011) 155–159, https://doi.org/10.1109/ EDM.2011.6006921.
- [27] L. Tadrist, H. Combeau, M. Zamoum, M. Kessal, Experimental study of heat transfer at the transition regime between the natural convection and nucleate boiling: influence of the heated wall tilt angle on the onset of nucleate boiling (ONB) and natural convection (ONC), Int. J. Heat Mass Tran. 151 (2020) 1–52, https://doi. org/10.1016/j.ijheatmasstransfer.2020.119388.
- [28] https://www.captec.fr/copie-de-accueil".

- [29] "Siemens Industries Digital Software. Simcenter STAR-CCM+, Version 18.06.006, Siemens 2018.".
  - [Online]. Available: https://engineeringtoolbox.com/.
- [31] M. Zamoum M, L. Tadrist, H. Combeau, Kessal, Experimental study of boiling heat transfer on multiple and single nucleation sites using a boiling-meter, Heat Transf. Eng. 35 (5) (2013) 508–516.
- [32] W. F. Thery P., D. Leclerq, "Device for Measuring the Intensity of a Radiative Flux and Optionally Also Measuring the Intensity of a Convective Flux," vol. 4,850,713.
- [33] Y.-A.H. Malika, Etude et réalisation de microcapteurs de flux thermique en technologie silicium. Université des sciences et technologies de Lille, France, 2007.
- [34] G. H., Réalisation d'un fluxmètre thermique à gradient tangentiel de température à paroi auxiliaire textile intégrant des fils thermoélectriques: application à la mesure des transferts thermiques et hydriques. Université des sciences et technologies de Lille, France, 2015.
- [35] FluxTeq." [Online]. Available: https://fr.fluxteq.com/.
- [36] 3M, Electronic Liquid FC-72, 2000, pp. 1–4 [Online]. Available: papers2://publication/uuid/78C1E9D4-6BFC-437D-995F-0B686829697A.
- [37] F.P. Incropera, D.P. DeWitt, Fundamentals of Heat and Mass Transfer, 1996, https://doi.org/10.1016/j.applthermaleng.2011.03.022.
- [38] Abdelkabir Zaite, Himanshi Kharkwal, Magali Barthe, L. Tadrist Lanzetta, Hervé Combeau, Thermal characterisation of a boiling meter using experiment and numerical simulation in a boiling cell, in: To Be Published in Lecture Notes in Mechanical Engineering, Springer, 2025.